

AD-A192 161

FAST ACTING OPTICAL BEAM DETECTION AND DETECTION
SYSTEMS UNIVERSITY COLL OF NORTH DAKOTA SCHOOL
OF ELECTRONIC EN. D K HAS-CH 18 87 DEC 87

1/1

UNCLASSIFIED

ARDC-R/D-4246-R-M2 DAJ845-83-C-0016

F/G 17/5

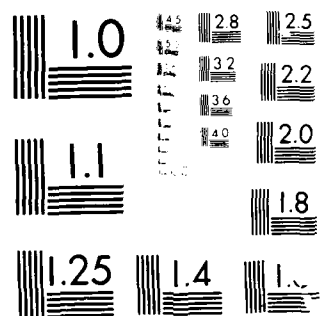
NL

END

DATE

FILED

87



MICROCOPY RESOLUTION TEST CHART
 NATIONAL BUREAU OF STANDARDS-1963-A

DTIC FILE COPY

(C) (X)

DOCUMENTATION PAGE

Form Approved
OMB No 0704-0188
Exp Date Jun 30, 1986

AD-A192 161

DTIC
ELECTE

FEB 24 1988

26. DECLASSIFICATION/DOWNGRADING SCHEDULE

1b. RESTRICTIVE MARKINGS

3. DISTRIBUTION/AVAILABILITY OF REPORT

Approved for public release; distribution unlimited.

4. PERFORMING ORGANIZATION REPORT NUMBER(S)

5. MONITORING ORGANIZATION REPORT NUMBER(S)

R&D 4246-R-MS

6a. NAME OF PERFORMING ORGANIZATION
University College of
North Wales

6b. OFFICE SYMBOL
(If applicable)

7a. NAME OF MONITORING ORGANIZATION
USARDSG-UK

6c. ADDRESS (City, State, and ZIP Code)
School of Electronic Engineering Science
Dean Street, Bangor,
Gwynedd, LL57 1UT

7b. ADDRESS (City, State, and ZIP Code)
Box 65
FPO NY 09510-1500

8a. NAME OF FUNDING/SPONSORING
ORGANIZATION
USARDSG-UK ARO-E

8b. OFFICE SYMBOL
(If applicable)

9. PROCUREMENT INSTRUMENT IDENTIFICATION NUMBER
DAJA45-83-C-0016

8c. ADDRESS (City, State, and ZIP Code)
Box 65
FPO NY 09510-1500

10. SOURCE OF FUNDING NUMBERS

PROGRAM ELEMENT NO.	PROJECT NO.	TASK NO.	WORK UNIT ACCESSION NO
61102A	1L161102BH57	00	

11. TITLE (Include Security Classification)

(U) Fast Acting Optical Beam Detection and Deflection System

12. PERSONAL AUTHOR(S)

Dr. D.K. Das-Gupta

13a. TYPE OF REPORT
Final

13b. TIME COVERED
FROM 1983 TO 1987

14. DATE OF REPORT (Year, Month, Day)
1987 December 7

15. PAGE COUNT
57

16. SUPPLEMENTARY NOTATION

microfilm

17. COSATI CODES

FIELD	GROUP	SUB-GROUP
09	03	
20	05	

18. SUBJECT TERMS (Continue on reverse if necessary and identify by block number)

idea Helium-Neon 3 deg micrometers

19. ABSTRACT (Continue on reverse if necessary and identify by block number)

The final report gives an account of progress made in the time period of January 1983 - December 1987 on Fast Acting Optical Beam Detection and Deflection System. It has been divided into two parts, each section being self-contained. Part 1 deals with the investigation of optical detection of coherent radiations of He-Ne laser of wavelength 0.6328 μ m with corona poled polyvinylidene fluoride (PVDF) film using its pyroelectric property. The results show that a detection time of 0.5 μ s may be achieved with PVDF pyroelectric detectors. Part 2 reports the results of acousto-optic deflection of coherent He-Ne laser radiations using a water-cell which was energised by well-poled PVDF film in the frequency range of 10 MHz-70MHz. 100% deflection efficiency of the primary beam energy has been achieved with this technique at a deflection angle of 1°. The water cell was then replaced with a Tellurium dioxide cell which provided 84% deflection efficiency at an angle of 3°. Finally, the report discusses a possible effective method of simultaneous deflection and deflection of coherent laser radiations with very high efficiency using blazed diffraction grating in the wavelength range of 0.4 - 1 μ m at angles 18° or more. Keywords: optical detect

20. DISTRIBUTION/AVAILABILITY OF ABSTRACT

☒ UNCLASSIFIED/UNLIMITED ☐ SAME AS RPT. ☒ DTIC USERS

21. ABSTRACT SECURITY CLASSIFICATION

Unclassified

22a. NAME OF RESPONSIBLE INDIVIDUAL
Dr. Wilbur C. Simmons

22b. TELEPHONE (Include Area Code)
01-409 4423

22c. OFFICE SYMBOL
AMXSN-UK-RM

DD FORM 1473, 84 MAR

83 APR edition may be used until exhausted
All other editions are obsolete

SECURITY CLASSIFICATION OF THIS PAGE

Unclassified

micrometers

1800

FAST ACTING OPTICAL BEAM DETECTION
AND DEFLECTION SYSTEM

U.S. ARMY - ERO CONTRACT NO. DAJA 45-83-C-0016
FINAL REPORT (DECEMBER 1987)

DR.D.K. DAS-GUPTA
SCHOOL OF ELECTRONIC ENGINEERING SCIENCES,
UNIVERSITY COLLEGE OF NORTH WALES,
DEAN STREET,
BANGOR,
GWYNEDD. LL57 1UT

88 2 22 217

PART 1: FAST OPTICAL DETECTION OF LASER RADIATIONS WITH
CORONA POLED POLYVINYLIDENE FLUORIDE (PVDF)

1.1. Introduction

A pyroelectric detector can be made with thin polymeric transparent film which is comparatively cheap, mechanically strong and chemically inert under hostile ambient conditions. The aim of this work was to use PVDF to detect a laser beam ($\lambda=0.6328\mu\text{m}$) in as short a time as possible, ideally within $1\mu\text{s}$.

1.2 Theoretical Approach to the Pyroelectric Response of PVDF Electret

An electret may be formed by applying a high electrical stress on a metal-dielectric-metal sandwich at an elevated temperature for an extended period of time and subsequently cooling the sandwich system to the ambient temperature in the presence of the external electric field (conventional poling) or by corona charging at ordinary temperature. The relationship between the dielectric displacement D , the electric field F and the frozen-in non-equilibrium polarisation P is given by:

$$D = \epsilon_0 \epsilon_r F + P \quad \dots (1)$$

where ϵ_0 and ϵ_r are the permittivity of free space and the relative permittivity of the dielectric material respectively. For $F = 0$, i.e., with a short circuited poled sample, we have¹ from equation (i):

$$\left| \frac{\delta D}{\delta S} \right|_{F=0, T} = \left| \frac{\delta P}{\delta S} \right|_{F=0, T} = \left| \frac{\delta(Q/A)}{\delta S} \right|_{F=0, T} \quad \dots (2)$$

$$= \frac{1}{A} \left| \frac{\delta Q}{\delta S} \right|_{F=0, T}$$

where S is the stress, Q the charge liberated, A the electrode area and T the temperature. The pyroelectric coefficient $p(T)$ may be expressed thus:

$$p(T) = \frac{1}{A} \left| \frac{\delta Q}{\delta T} \right|_{F=0, S} = \frac{1}{A} \frac{\delta Q}{\delta t} \frac{\delta t}{\delta T} \quad \dots (3)$$

$$= \frac{1}{A} I \frac{\delta t}{\delta T}$$

where I is the short-circuited current through the sample and $\delta T/\delta t$ is the rate of rise of temperature.

When an electret is used as a pyroelectric detector, it must absorb some of the incident radiation. As a result, the material undergoes a temperature change, which in turn changes the spontaneous polarisation, generating an electrical signal. If we assume that the radiation gives rise to a uniform and a small temperature rise T , the heating effect will be governed by the differential equation:

$$C_T \left| \frac{d(\Delta T)}{dt} \right| + G_T \Delta T = AB(t) \quad \dots (4)$$

where C_T is the thermal capacity of the crystal structure which is proportional to its density, specific heat capacity and volume, G_T is the thermal conductance of the supportive apparatus (radiative, convective and conductive), A is the exposed electroded area of the sample and $B(t)$ is the power absorbed per unit area of the material. The right hand side of equation (4), therefore, represents the total power absorbed. A temperature change of the form described by equation (4) will give rise to a pyroelectric surface charge, given by:

$$\overline{\sigma}_s = \frac{|\delta P \cdot n|}{|\delta T|} \Delta T = p(T) \Delta T \quad \dots (5)$$

where $\overline{\sigma}_s$ is the pyroelectric surface charge density (Cm^{-2}) and n the unit vector normal to the surface. The pyroelectric current density is given by the time derivative of equation (5), i.e.,

$$J = p(T) \frac{\delta T}{\delta t} \quad \dots (6)$$

If we take into consideration of the effect of the measuring apparatus, the equation for the charge flow becomes:

$$C \frac{dV}{dt} + \frac{V}{R} = p(T) \frac{dT}{dt} \quad \dots (7)$$

where C and R are the combined capacitance and resistance of the sample and the measuring equipment and V the voltage developed across the sample. It may be assumed that the pyroelectric coefficient, the dielectric constant and the specific heat of the material remain constant for small ΔT . Above equations may be used to show that the current response is given by^{2,3}.

$$I(t) = \frac{B_0}{\rho} \frac{Ap(T)}{C_p a} \frac{(1)}{(1-\theta)} \left| (\exp -t/\tau_T) - (\exp -t/\tau_E) \right| \quad \dots (8)$$

where B_0 is the radiation power absorbed per unit area of the electroded material, ρ the density of the material (Kg. m^{-3}) C_p the specific heat ($\text{JKg}^{-1}\text{OC}^{-1}$), a the sample thickness (m), θ is τ_E/τ_T , τ_E is the electrical time constant of the system ($=RC$) and τ_T is the thermal time constant of the system ($=C_T/G_T$, $C_T = \rho C_p a A$). Here it has been assumed that $\tau_E = \tau_T$. Equation 8 represents the difference between two exponentials with the same initial value, but decaying with two time constants (See Figure 1). The peak value of the pyroelectric current I_p , the time t_p for the pyroelectric current to reach this value and the initial slope K of the pyroelectric response to a step input of radiation are given by²:

$$I_p = \frac{B_0 p(T) A}{\rho C_p a} \cdot \theta \frac{\left(\frac{\theta}{(1-\theta)} \right)}{(1-\theta)} \quad \dots (9)$$

$$t_p = \tau_E \ln \left(\frac{\theta}{(1-\theta)} \right) \quad \dots (10)$$

$$\text{and } K = \left| \frac{dI(t)}{dt} \right|_{t=0} = \frac{|B_{op}(T)A|}{|\rho C_p a|} \frac{(1)}{(\tau_E)} \quad \dots (11)$$

The shape and the speed of the pyroelectric response are largely dependent on τ_E and τ_T . Figure 2 shows the equivalent circuit of sample and electrometer from which it may be observed that the dominant parameters to affect τ_E are the sample capacitance C_S and the effective resistance of the measuring apparatus R_A . Now:

$$C_S = \frac{\epsilon_0 \epsilon_r A}{a} \quad \dots (12)$$

Thus to reduce C_S , A should be reduced for a chosen material. R_A may be altered by applying feedback.

Thus to summarize, the dominant parameter which affect the electrical time constant are the effective capacitance of the system (i.e. the sample capacitance together with other capacitance between the samples and the amplifier) and the effective resistance of the amplifier and the measuring system. The effective resistance may be altered by a judicious selection of an output amplifier. The sample capacitance may be reduced by an appropriate choice of electrode area and the sample thickness. The thermal time constant (=thermal capacitance/thermal conductance) is dependent on the sample holder. The thermal capacitance is dependent on the sample area and thickness, whereas the thermal conductance is dependent on the conductive, convective and the radiative properties of both the sample and the sample holder. The greater the difference between the two time constants, the greater is the probability that the shorter time constant (i.e., the electrical time constant in the present case) will determine the rise time of the pulse, whilst the longer time constant will determine the decay of the pyroelectric signal². The thermal capacity C_T ($= C_p \rho a A$) may be reduced by reducing the sample thickness a and the electrode area A . However, a reduction in the value of a will increase the sample capacitance C_S and hence a compromise is needed in the choice of the values of a and A to minimise C_S and C_T .

1.3 Experimental Procedure

Uniaxially stretched 9 μm thick Kurete PVDF films, mostly of polar form 1 structure were corona poled at 100°C with a field of $2.2 \times 10^8 \text{ Vm}^{-1}$. A limiting factor to a fast rising pyroelectric signal from the detector would be the noise content of the response. One of the noise sources was observed to be the thickness of the vacuum deposited aluminium electrodes. Below a thickness of 50Å for the electrodes the noise current of the pyroelectric signal increased quite significantly. The optimum thickness for the rear electrode was observed to be 300Å whereas the corresponding figure for the front electrode was 100Å. It became apparent that to obtain a maximum pyroelectric response of a suitably poled sample, the electrode area needs to be kept to a minimum value and the total electrode thickness should be approximately 400Å, as stated above. One of the electrode configurations which would meet these constraints and still allow

a good transmission of the incident radiations and provide a significant response over a large sample area would be a matrix arrangement. A 30 element grid matrix of aluminium electrode assembly (figure 3) was vacuum deposited on each face of the sample using a specially prepared mask. The sample was then mounted on a suitable holder with PCB backing.

It was considered necessary for the detector to provide a pyroelectric signal of sufficient magnitude to activate a protection system against an incoming harmful radiation in the early stages of the rise of the pyroelectric signal. It was necessary to use an operational amplifier with a very high open loop gain, extremely low input noise voltage and bias current 200 nA and a fast slewing rate. An amplifier which meets the above requirements well is AD515K of Analog Devices Limited and this has been used in the present work. The operational amplifier was mounted on a PTFE base as close as possible to the PVDF film. Figure 4 shows the equivalent circuit of the sample and the current amplifier (AD 515K) together with its feedback resistor (10^{10} ohms).

For the switching network to activate a protection device, it was decided to use a comparator circuit. Comparators come in integrated circuit (IC) form usually, and the output switches from logic 1 to logic 0 when the input voltage crosses predetermined threshold voltage, set at the second input to the device. The logic output is the main reason for choosing comparators to do the switching, as a digital signal is very much easier to interface with a subsequent circuit to activate a protection (i.e. deflection) system at a low cost.

As the pyroelectric effect is a reversible one, the signal can have a positive or negative polarity, depending on whether the electret is being heated or cooled. Hence one comparator indicates the recent incidence of a laser beam, and the other shows its recent removal. The word 'recent' is used as the output from the amplifier will only stay above the threshold value for a finite time, the response decaying to zero if no further change in temperature occurs. A deflection system would need to be activated continuously until a 'laser-off' signal is received. This necessitates an inclusion of a latching circuit, made from two T.T.L. NAND gates. If A is the 'laser-on' comparator output and B is the 'laser-off' comparator output and recalling that a detection gives a logic '0', a typical sequence of events is as follows

	A	B	Q	
	1	1	?	} System activated.
Laser on	0	1	1	
	1	1	1	
Laser off	<hr/>			
	1	0	0	
	1	1	0	

When the detector system is first turned on, the latch is in the ambiguous state, and Q be either 0 or 1. For this reason a push button switch is incorporated in the circuit which introduces a '0' at the B input, resetting the latch. This need only be used after a power failure or if the input should trigger without due course. The complete pyroelectric detection system has been built on PCB and is shown in figure 4.

A spectra Physics model 159 He-Ne laser was used as the radiation source. Arrangements were incorporated to modulate the laser beam by an electromechanical chopper blade system which may be driven in the frequency range of 0.5 Hz to 1 KHz. A camera shutter assembly was used with a Cannon F.P. model II camera to provide a single step input of laser radiations. The noise level of the pyroelectric response was investigated using a Spectral Analyser (Marconi Model TF 2370 with a zero loss probe TK 2374) which covers a frequency range of 30 Hz to 110 MHz with sweep widths varying from 5 Hz to 5KHz. A Tektronix storage oscilloscope with an input impedance of $1M\Omega$ and input capacitance of $27\mu F$ together with plug-in amplifier type 1A7 was used for the present work.

1.4 Results and Discussion

1.4.1 Preliminary Observations of the Illumination Properties of the Modulated Laser Beam

In order to establish the rise time of a chopped laser pulse, a photoelectric detector with a response time of $10 \times 10^{-12} s$ was used. A knowledge of the number of blades of the electromechanical chopper and their axial distance from the centre of the driving motor shaft to the laser beam allowed the blade velocity to be calculated from the period of the resulting waveform. The experimentally observed values of the rise time of the photo detector current to its peak value for different blade velocities together with the calculated values are shown in figure 5. These measurements were made with a restricted beam diameter of 0.8mm. It may be observed from figure 5 that the experimental results are in agreement with their respective calculated values which assumed that the motor speed was linear at all settings of the energising current and that the angle of incidence of the laser beam on the photodiode was consistent.

The effect of the laser beam area or the rise time of the photodetector current was determined using suitable apertures of diameters in the range of 0.4 mm to 1.4 mm at a chopping frequency of 25 Hz. The results (figure 6) show that faster rise times were obtained with decreasing beam diameters. However, the response was observed to be greatly distorted by noise for beam diameters less than 1 mm, probably resulting from minor misalignment of the aperture with respect to the central area of the beam.

1.4.2 Pyroelectric PVDF Detector Response

Considerable efforts have been made in the present work to arrive at an optimum geometry of electrode (i.e. area and thickness). Initially a single electrode of identical area on each sample face was employed to determine the effect of electrode area on the amplitude of the pyroelectric response at 1 ms using a step input of incident radiation. It may be observed from figure 7 that the pyroelectric response decreased with increasing electrode area.

Furthermore, the initial rate of rise of the response also decreased with increasing area of the electrode. It may be expected that the initial rate of response and the peak amplitude of the pyroelectric signal should increase with increasing electrode area provided the laser radiation is uniform over the whole area. However, the thermal energy of the laser beam varies in a Gaussian manner from the centre of the beam towards its periphery. As a result, an increase in the electrode area reduces the average energy per unit area of the active electrode system. The lower limit of the active area may, however, be limited by dependence on the lateral heat conduction of the surface.

Figure 8 shows the effect of front electrode thickness on the pyroelectric response of corona poled PVF_2 with three different thicknesses (50Å, 100Å and 300Å) of the rear electrode. A thinner electrode on the front face increased absorption of thermal energy, whilst a thicker electrode on the rear face increased reflection. Thus from a theoretical approach such a system of electrodes, as described above, should provide an increase of pyroelectric responsivity which it did although in a non-linear manner. Duffy⁴ has shown that the resistance of an evaporated electrode increases rapidly with thicknesses below 50Å. This effect would explain the observed increase in noise and apparent decay in responsivity due to an increase in the effective electrical time constant of the measuring system. The noise content is almost certainly due to Johnson noise arising from the granular nature of the thin electrodes. Throughout the definitive experiments in the present work the rear electrode was of 300Å evaporated aluminium while the thickness of the front electrode was 100Å.

It is apparent from above discussion that for maximum pyroelectric responsivity the electrode area should be kept to a minimum and the total electrode thickness is not to be less than 400Å. An electrode configuration which would meet these constraints and still allow good transparency as well as give a pyroelectric response over a large area, would be matrix. An optimum spacing of 0.2 mm was established from experimental observations for the matrix elements of electrodes. An increased spacing produced a significant decay in responsivity whilst a reduction from 0.2 mm provided increased noise. The final electrode configuration, used in the present work, consisted of an array of 30 elements on each face of a sample, arranged in a cross-hatch pattern (figure 3), the matrix elements on each side being shorted at each end. The resulting peak response, as stated earlier, was 0.03V compared to 0.002V for a conventional fully electroded sample. The improvement gained by such a matrix electrode system must be due to a decrease in electrical capacitance and a reduction of Johnson noise.

A study of electrical noise was carried out using a spectrum analyser which indicated that the major source of noise was the mains frequency at 50 Hz. A Butterworth bandpass filter was designed (figure 9) using low pass and high pass circuits in cascade with cut-off frequencies at 50Hz and 100 Hz respectively. It may be observed from figures 10(a) and 10(b) that the use of such a filter network removed the electrical noise content very

significantly from the pyroelectric response. However, this filtering affected the rate of rise of the initial response. By a careful choice of bandwidth a pyroelectric response of $10\mu\text{V}$ was obtained at $5\mu\text{s}$.

It may be shown^{5,6} that the normalised responsivity r of a pyroelectric detector is given by:

$$r = w (\tau_T + \tau_E)^{-1} (1 + w^2 \tau_E^2)^{-1} \dots (13)$$

where τ_T and τ_E are the thermal and electrical time constants respectively and w the angular frequency of modulation (i.e. chopping rate) of the incident radiation.

For $w\tau_E \gg 1$ (i.e. high frequency case),

$$r = (\tau_T + \tau_E) (w\tau_T\tau_E)^{-1} \dots (14)$$

At low frequencies (i.e. $w\tau_E \ll 1$),

$$r = w(\tau_T + \tau_E)^{-1} \dots (15)$$

If the two time constants differ by more than an order of magnitude,

$$r = (w \tau_{\min})^{-1} \text{ for } w\tau \gg 1 \dots (16)$$

and

$$r = (w \tau_{\max})^{-1} \text{ for } w\tau \ll 1 \dots (17)$$

The values of τ_E and τ_T may be obtained from a measurement of r over a suitable range of frequencies using equations 14, 15, 16 and 17. The responsivity of the PVF₂ pyroelectric detector was obtained over a frequency range of 0.5 Hz to 70 Hz. To test the response time, the logic comparator circuitry (figure 4) was used to trigger a logic pulse at times of 200, 400, 600 and 800 nanoseconds. The pyroelectric response and the logic output were compared using a twin beam Tektronix oscilloscope. To find the voltage level needed at the comparator to achieve these times, the pyroelectric response was first displayed on the oscilloscope and the voltage was noted at required times.

Figure 11 shows the results of measurement of responsivity in the frequency range of 0.5 Hz to 70 Hz using the method discussed above. It may be observed that a maximum responsivity of 515 V W^{-1} for a 30 element cross-hatch detector grid matrix was obtained in the present case at a chopping frequency of 1.5 Hz for a cornea poled PVF₂ film of $9 \mu\text{m}$ thickness. The electrical and the thermal time constants were observed to be $58.5 \times 10^{-3} \text{ s}$ and 242 s respectively. It was observed that the thermal conductivity is far greater for a multiple array of electrodes than for a single array which may be due to an enhanced lateral conduction for the former case on the detector surface.

Finally, figure 12 shows an actual pyroelectric response of the PVF₂ detector with 30 element electrode matrix assembly for a step input of incident laser (He-Ne) radiation from which it may be observed that sufficient output voltage is available to trigger an acousto-optic deflector system in a time of approximately 0.5 μ s. In order to obtain this rise time a camera shutter speed of 1/1000th second was used. A further reduction of triggering time may be obtained by the use of more expensive and sophisticated design of electronic amplification system. A reduction in pressure of the pyroelectric detector assembly environment resulted in an exponential increase in responsivity and a decrease in noise level. The initial rate of increase in response, however, showed little improvement. Further work is necessary in these aspects.

1.5 Conclusion

Using corona poled PVDF with 30 element grid structure for electrodes, a detection and a subsequent warning for the harmful coherent laser radiations (He-Ne: $\lambda=0.63\mu\text{m}$) may be provided in 0.5 μ s.

References

1. Das-Gupta, D.K. and Doughty, K., J. Phys. D., 11, 2415 (1978).
2. Simhony, A. and Shaulov, A., J. Appl. Phys., 42, 3741 (1974).
3. Das-Gupta, D.K. and Doughty, K., J. Appl. Phys., 51 1733 (1980).
4. Duffy, J.S., Ph.D. Thesis, University of Wales (1983).
5. Cooper, J., J. Sci., Instrum., 39, 467 (1962).
6. Putley, E.H., Infrared Physics, 2, 139 (1973).

Legends

- Figure 1 Theoretical plot of pyroelectric current response with normalized time.
- Figure 2 Equivalent circuit of the sample and the current amplifier (AD515K).
- Figure 3 Grid matrix of the electrodes
- Figure 4 Pyroelectric detection system
- Figure 5 Photo detector current rise time/blade velocity (One hundred blade modulator) with a laser beam of diameter 0.8 mm.
- Figure 6 Photo detector current rise time/laser beam diameter
- Figure 7 Pyroelectric response of corona poled PVDF at 1 ms/electrode area.

- Figure 8 Effect of front electrode thickness on pyroelectric response of corona poled PVDF.
- Figure 9 A fourth order low pass Butterworth active filter
- Figure 10 (a) Pyroelectric signal with a bandpass filter in the range DE-10 kHz.
 (b) Pyroelectric signal with a bandpass filter in the range >50 Hz to 10 kHz.
- Figure 11 Responsivity of PVDF pyroelectric detector with 30 element electrode grid matrix in the frequency range of 0.5 Hz to 70 Hz.
- Figure 12 Pyroelectric response of PVDF detector with an array of 30 electrode (grid matrix) and a step input of He-Ne radiations.

Fig. 1. Theoretical plot of the pyroelectric current response against time (normalized).

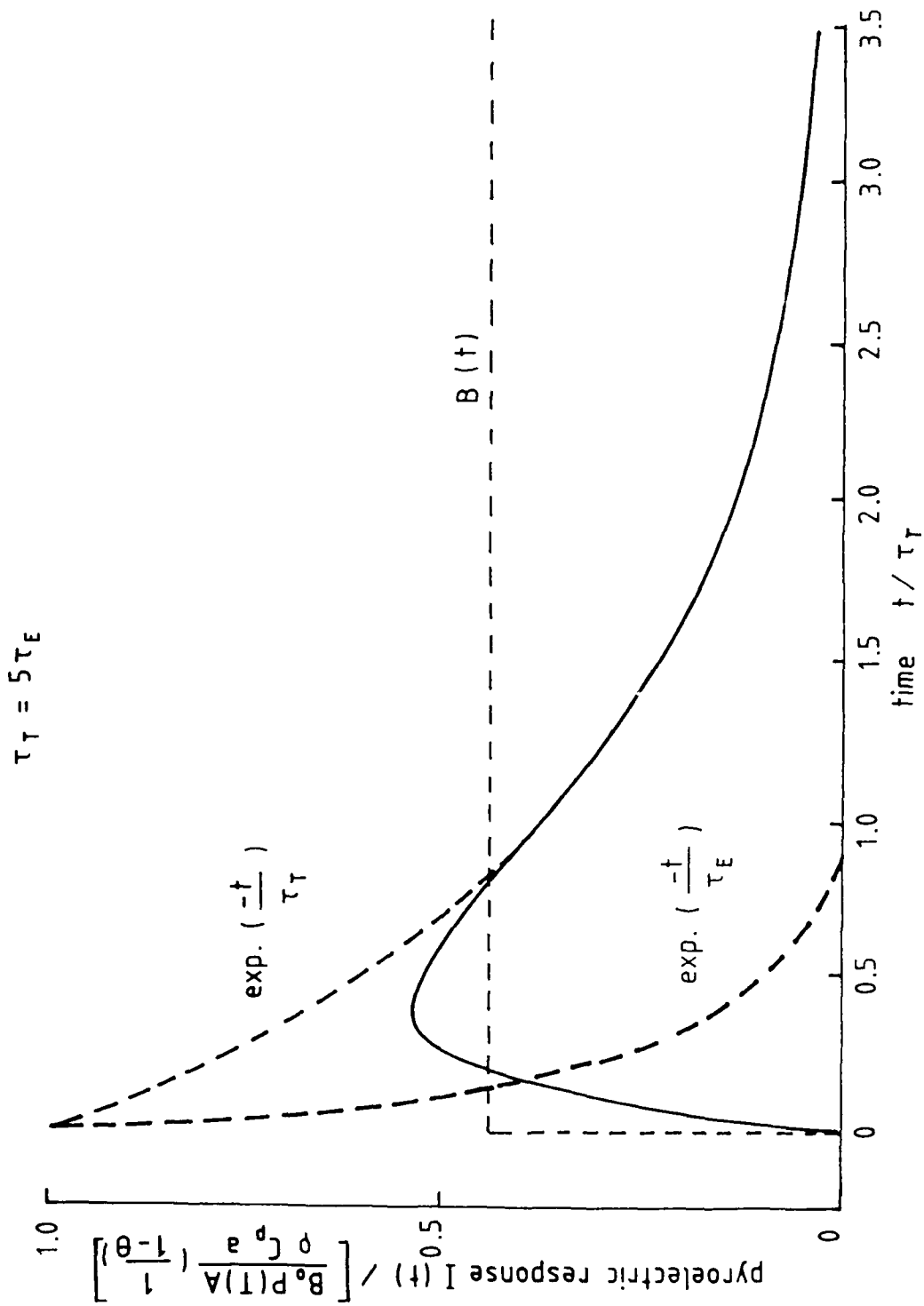


Fig. 2. Equivalent circuit of the pyroelectric sensing element and the current amplifier (AD515K).

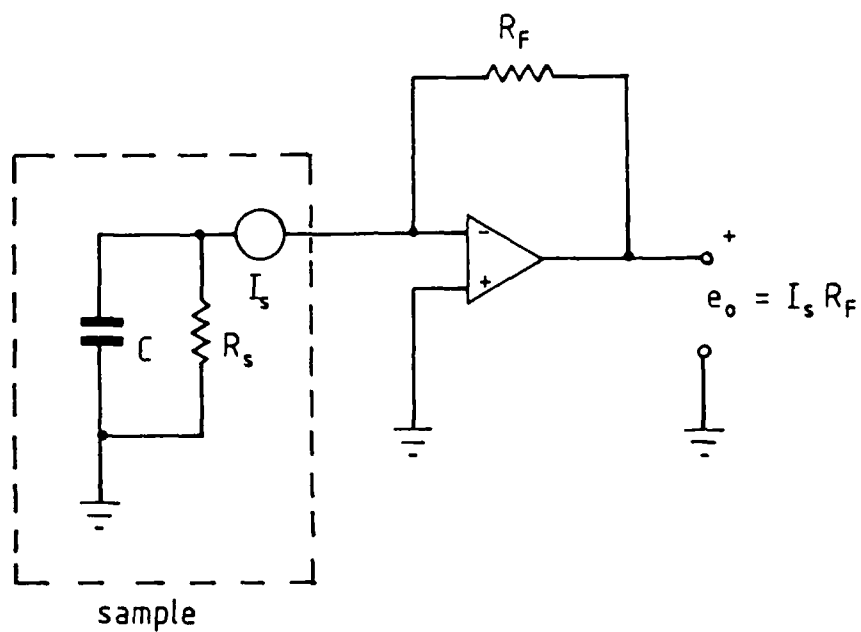


Fig 3. Matrix array of evaporated aluminium electrode elements on PVF_2 (30 elements on each face of the sample).

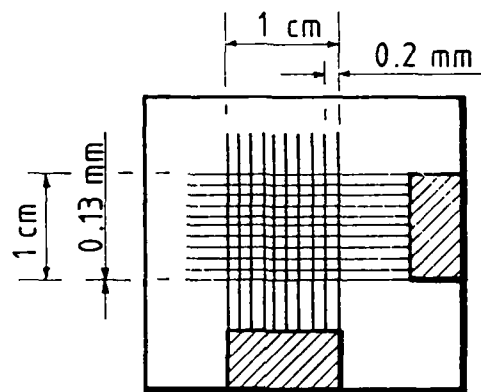


Fig. 4. Pyroelectric detection system with PVF₂ as sensing element.

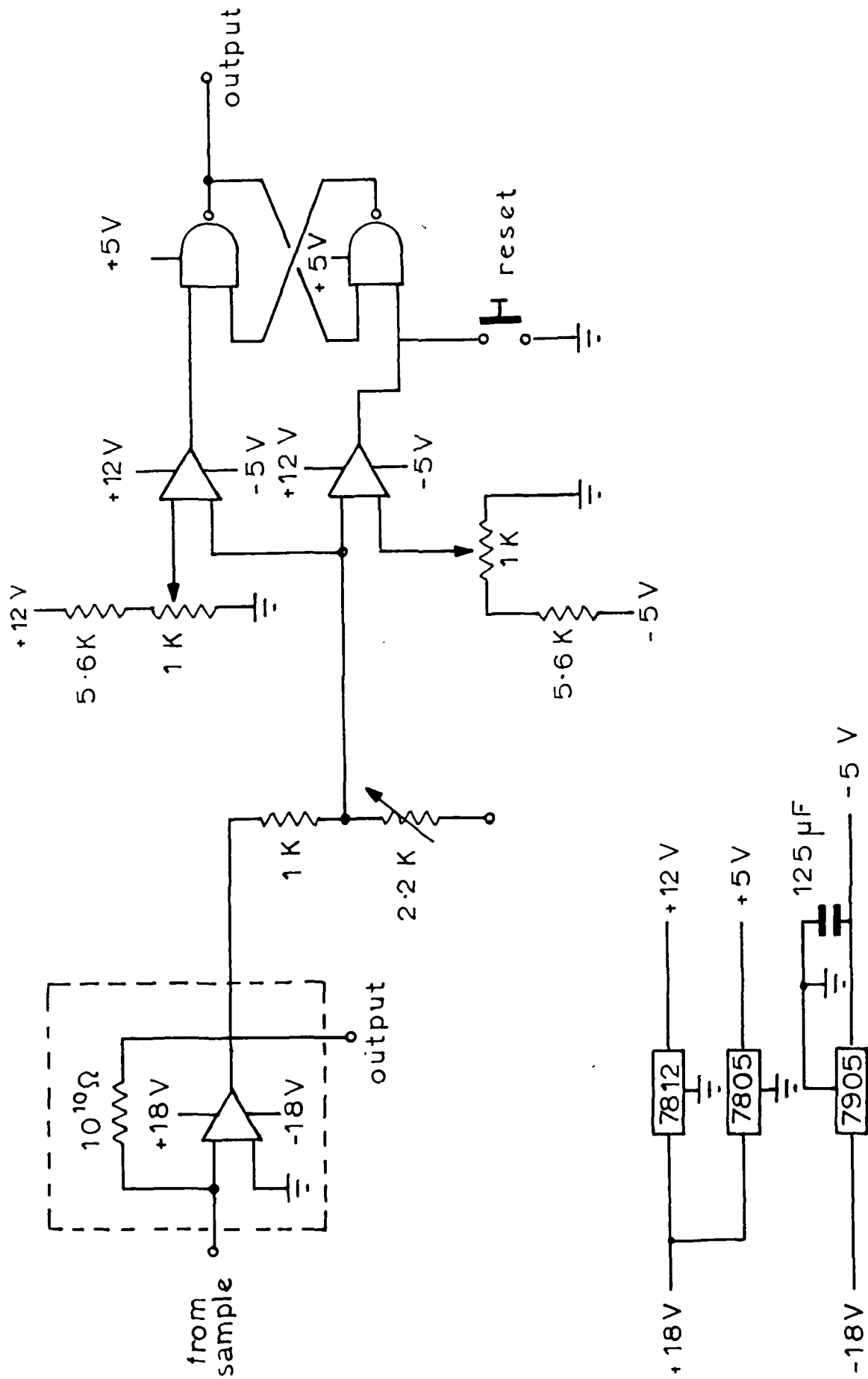


Fig.5 . Photo detector current rise time/blade velocity
(one hundred blade modulator) with a laser
beam diameter of 0.8 mm.

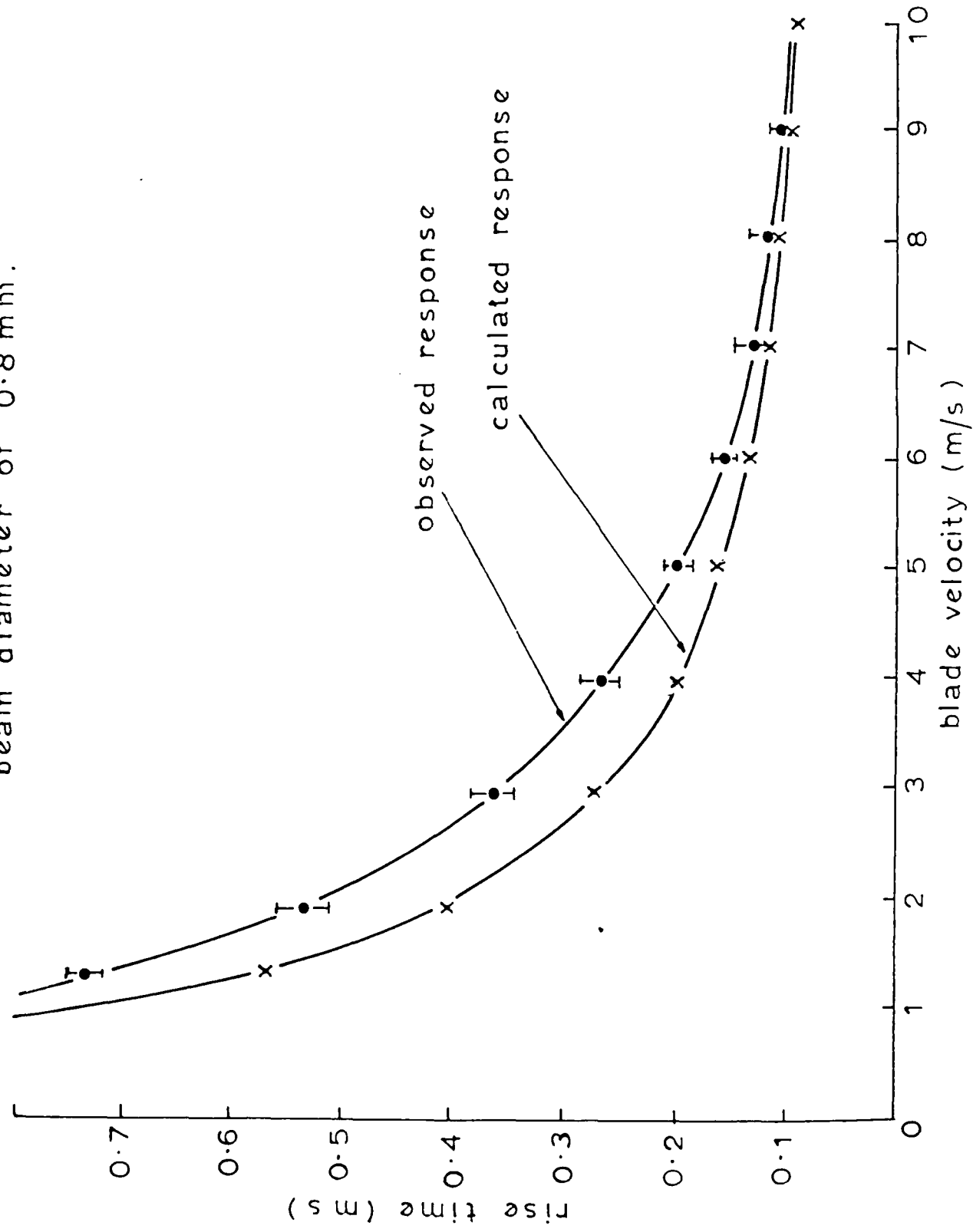


Fig. 6 . Photo detector current rise time / laser beam diameter.

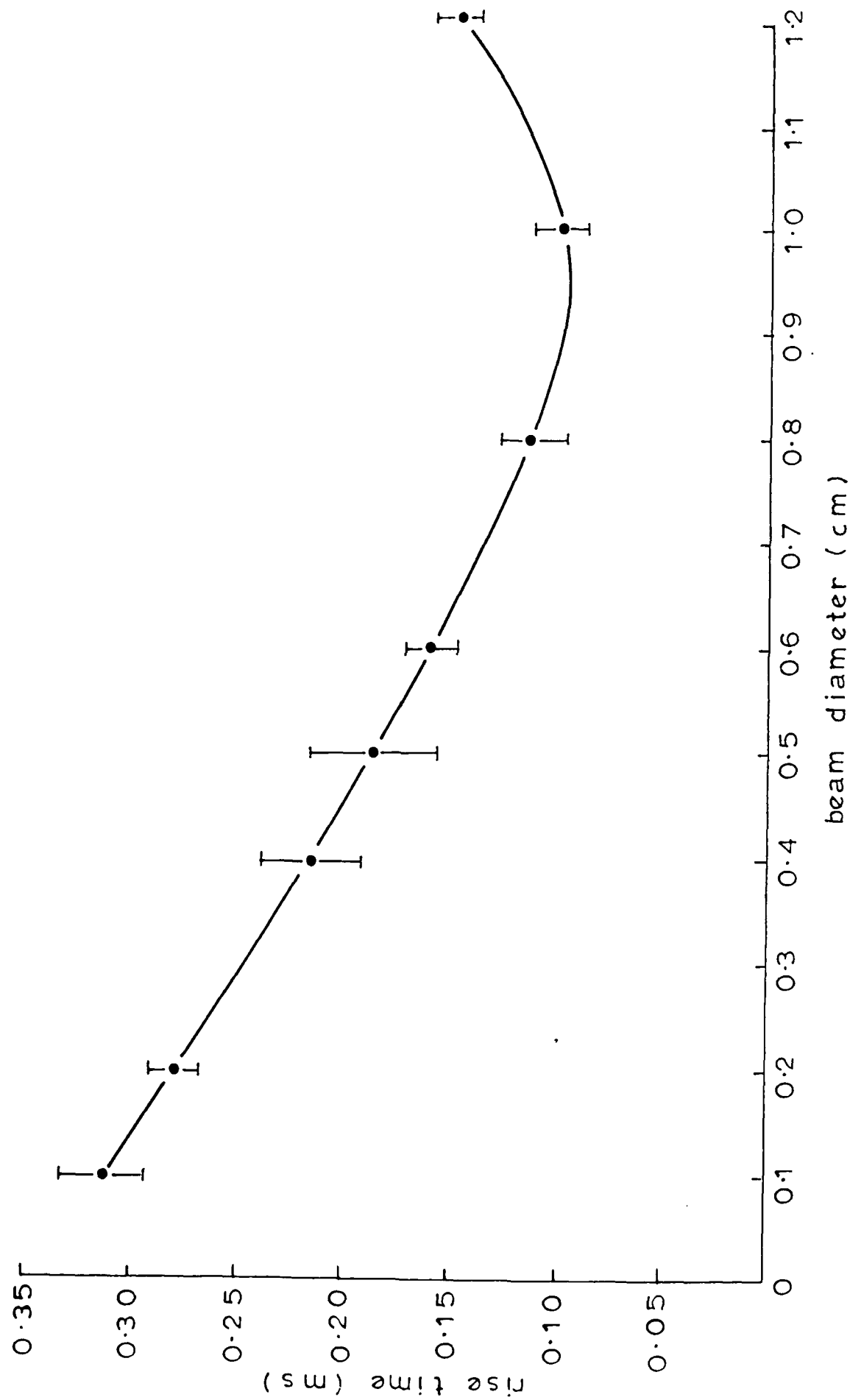


Fig. 7. Pyroelectric response of PVF₂ detector at
1ms / electrode area.

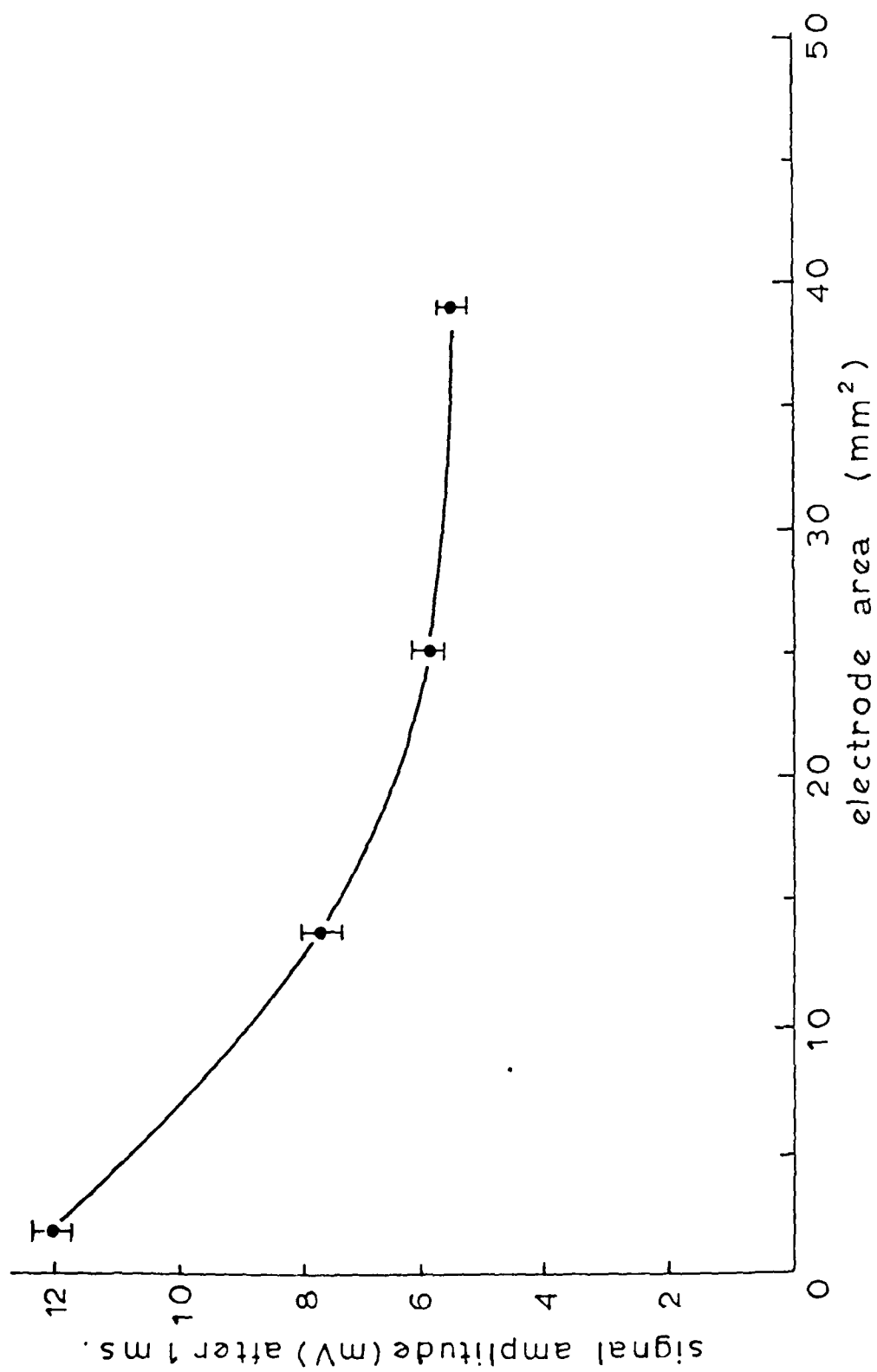


Fig. 8. Effect of front electrode thickness on the pyroelectric response of PVF_2 detector.

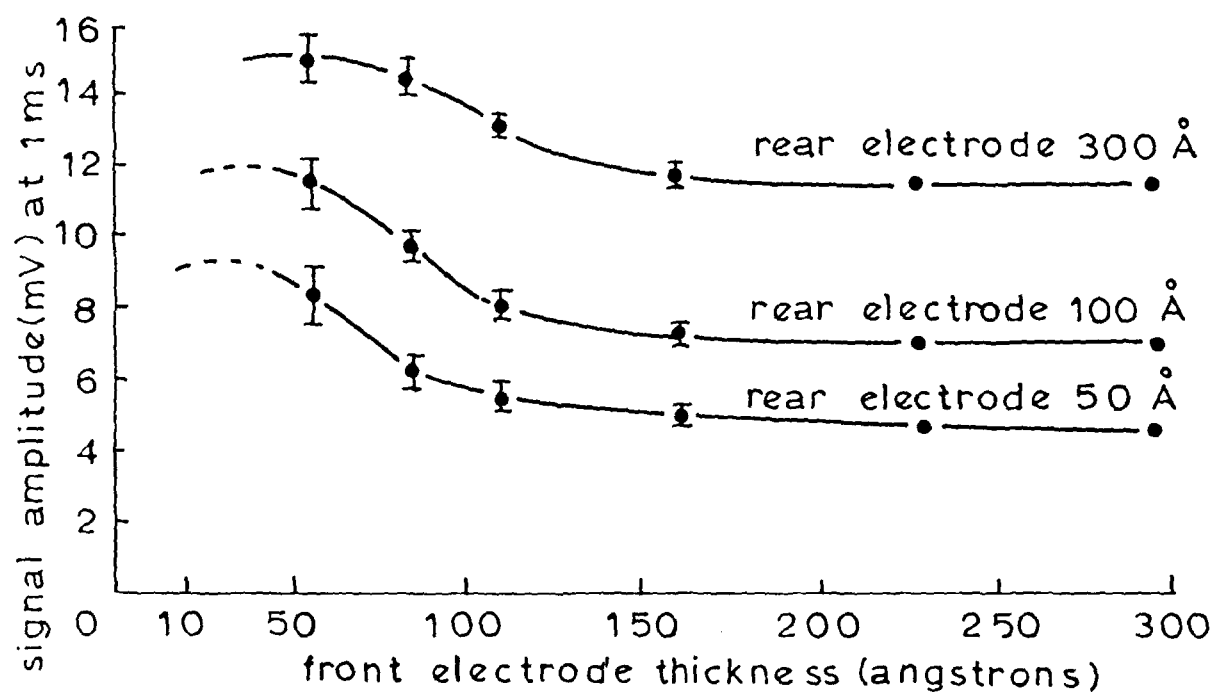
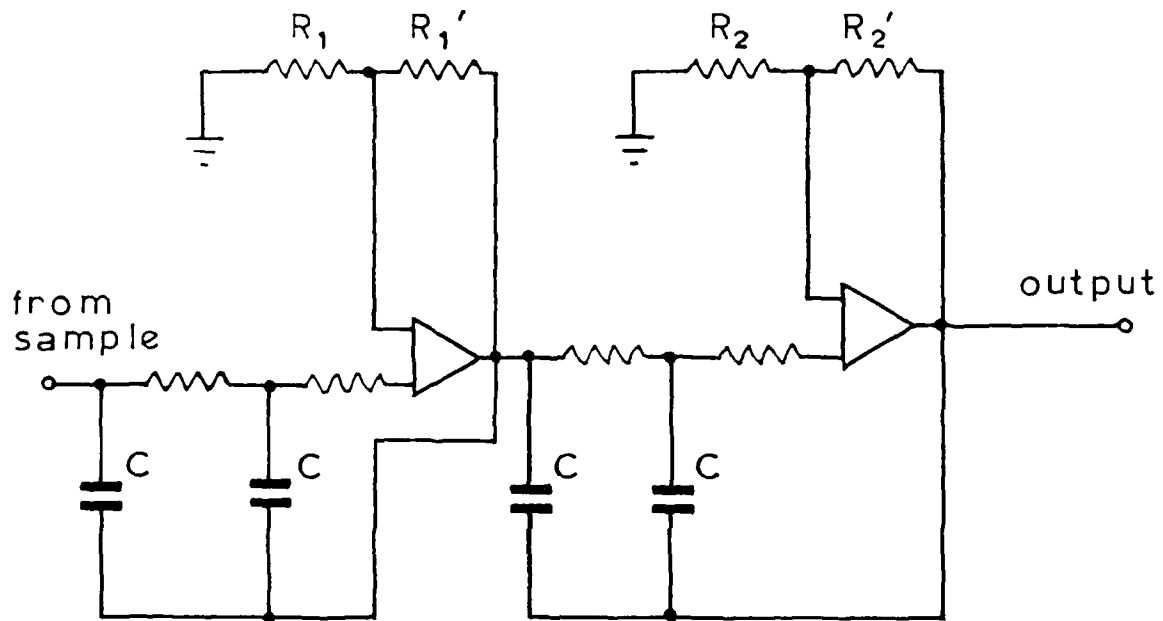


Fig.9. A fourth order low-pass Butterworth active filter.



Design summary

To transform to high-pass, the R & C's of figure 8 were interchanged. A bandpass filter was constructed using a low-pass and high-pass in cascade.

Values for R_1 R_1' R_2 & R_2'

Butterworth Polynomial $(s^2 + 0.765s + 1)(s^2 + 1.848s + 1)$

$$A_{V1} = 3 - 2k_1 = 3 - 0.765 = 2.235 = (R_1 R_1' / R_1) \Rightarrow R_1 = 10k, R_1' = 12.35k$$

$$A_V = 3 - 2k = 3 - 1.848 = 1.152 = (R_2 R_2' / R_2) \Rightarrow R_2 = 10k, R_2' = 1.25k$$

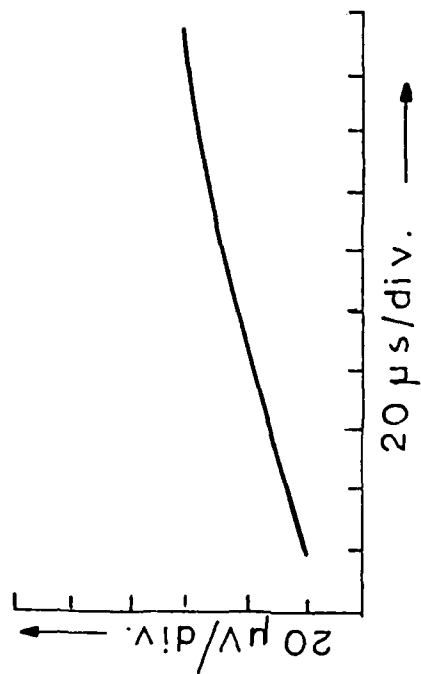
Values of R & C for cut-off frequencies

$$\omega_{OL} = \frac{1}{RC} \text{ at } 50 \text{ Hz } R_3 C = 3.18 \times 10 \Rightarrow 6800 \text{ pf. } 500k \Omega$$

$$\omega_{OH} = \frac{1}{RC} \text{ at } 100 \text{ KHz } R_3 C = 16 \times 10 \Rightarrow 3.3 \text{ pt. } 500k \Omega$$

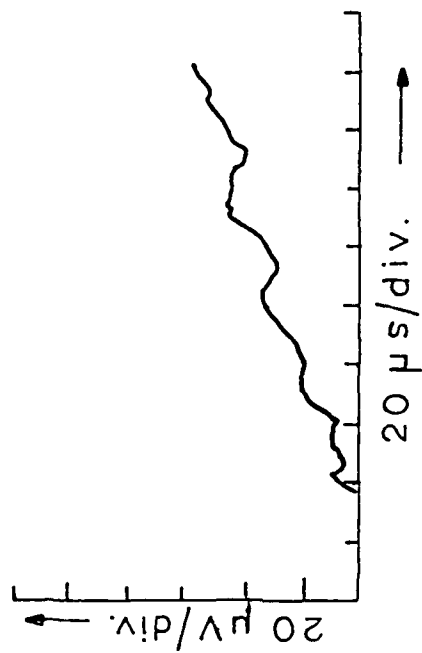
Fig. 10.

bandpass filter 50Hz/10KHz



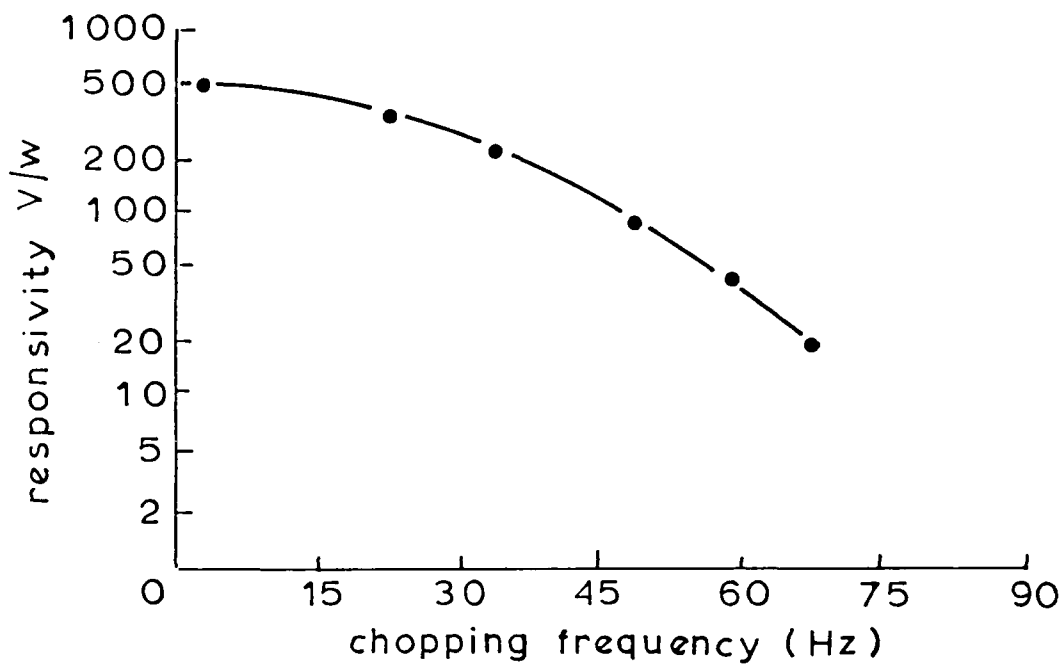
(a) Pyroelectric signal of
PVF₂ detector with bandpass
filter (>50Hz -10 KHz)

bandpass filter DC - 10 KHz



(b) Pyroelectric signal of PVF₂
detector with bandpass
(DC - 10 KHz)

Fig. 11. Responsivity of PVF₂ pyroelectric detector with an array of 30 electrodes (grid matrix) in the frequency range of 0.5 Hz to 70 Hz.



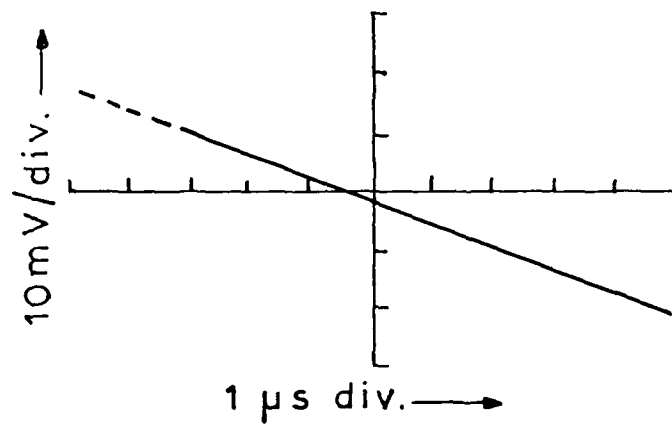
receiving area	0.05 mm ²
thickness	9 μm
responsivity at 70Hz	20 mV.
max. responsivity	515 mV at 1.3 Hz.

calculated parameters

τ_e from equation = $58.5 \times 10^{-3} \text{ s}$

τ_r from equation = 242 s

Fig. 12. Pyroelectric response of PVF_2 detector with an array of 30 electrodes (grid matrix) and a step input of He-Ne laser radiations.



Part 2 Theory and Practice of Acousto-Optic Interaction of Light

2.1 Introduction

When a transparent medium is subjected to a stress, the optical refractive index of the medium changes. High frequency sound waves, propagating through a transparent material via a piezoelectric transducer, will provide a periodic change in the refractive index of the material. In effect, sound waves produce a diffraction grating (Fig. 1) capable of diffracting incident coherent light. Diffraction of light by high frequency sound waves is called Brillouin Scattering [1]. The two most important forms of Acousto-optic interaction are Debye-Sears effect and Bragg diffraction.

2.2 Theory

2.2.1 The Debye-Sears Effect

Consider a plane wave of light, of angular frequency ω travels through a slab of material of length L (see figure 2). Let n be the refractive index of the material of the slab. Then the velocity of light in the slab is reduced from its vacuum value C to C/n and the wavelength λ of the light in the slab is:

$$\lambda = 2\pi C / \omega n \quad \dots (1)$$

The propagation constant β (i.e. the number of waves per 2π units of length) is given by:

$$\beta = \omega n / C \quad \dots (2)$$

The slab acts like an optical delay line with time delay,

$$\tau = n / C \quad \dots (3)$$

and phase shift:

$$\phi = L\beta \text{ radians} \quad \dots (4)$$

Let us now assume that we can change the refractive index n of the material by a small amount Δn . In so doing we vary the time delay and it would lead to the following phase excursion at the output,

$$\Delta \phi = L \Delta \beta = L \beta \frac{\Delta n}{n} = \frac{2\pi L \Delta n}{\lambda_0} \quad \dots (5)$$

where λ_0 is the vacuum wavelength of the light. For $\lambda_0 = 0.633$ micron (He-Ne laser) and $L=2.5$ cm, the factor L/λ_0 is about 4×10^4 . Thus a change in refractive index of only $\Delta n = 10^{-6}$ causes one-quarter radian of phase excursion. In other words, small change in phase velocity would produce a large change in phase shift at the receiving end.

Let us now assume that we can vary Δn sinusoidally at the modulation frequency ω_s . This may be conveniently done by applying a transducer at the bottom of the slab delivering sinusoidal plane wave in a vertical direction. This then has the effect of varying the density sinusoidally and this to a first order approximation, is equivalent varying the refractive index sinusoidally (see figure 3).

If the frequency of the sinusoidal variation of Δn is f_s (acoustic transducer frequency) then the output light emerging from the right hand side of the slab is now phase modulated at ω_s with maximum phase excursion as described by equation 5. A phase modulated wave is composed of a carrier and of side bands spaced ω_s away from the carrier and from each other (see figure 4).

Let us now consider the case of a large number of slabs similar to the one just described, stacked on top of each other. Each slab represents a quarter wavelength position of the compressional wave passing upwards through them, of frequency f_s . At a given instant a specific slab is compressed and its refractive index increases. One-half cycle later, it is dilated and its refractive index dilated. Thus the compressional wave is accompanied by a continuous wave of refractive index variation, both waves travelling upward together at the sound velocity V_s (see figure 5).

A plane wave of light of frequency w , travelling horizontally from left to right, impinges upon the left boundary of the column. Such slab modulates the light as before and so there will be carrier and sideband components all along the right hand side of the column. The carrier components, although changed in amplitude and perhaps reversed in polarity (if the phase excursion ϕ exceeds 2.4 rad) have the same phase for all slabs. Hence what remains of the light at the original frequency w , proceeds as optical carrier wave towards the right in the original direction. The situation is different for the upper side band $w + \omega_s$. In each slab, the phase of this sideband corresponds to the phase of the acoustic modulation that generated it, and that varies linearly from slab to slab as a function of vertical position, going through one complete cycle between the two slabs marked by the dashed line, which are one acoustic wavelength apart (see figure 5).

To find the direction in which sideband light of frequency $w + \omega_s$ is radiated, we construct a wavefront by connecting points of equal phase together (figure 5). Near the lower portions of the column, where the sound wave passed earlier and the phase is further advanced, such points move further to the right, one wavelength λ of the light horizontally for each wavelength Λ of sound vertically. The wavefront is therefore tilted by an angle as shown:

$$\tan \theta = \frac{\lambda}{\Lambda}$$

$$\text{or } \theta = \frac{\lambda}{\Lambda} \text{ as } \lambda \ll \Lambda \quad \dots (6)$$

The direction of propagation, which in isotropic substances must always be perpendicular to the wavefront, is deflected upward by the same angle. Wavelengths λ and Λ must be measured within the medium that carries the sound wave. If the angle of diffraction is measured in air ($\lambda = \lambda_0$), assuming that the light beam enters the ultrasound beam normal to its direction of travel, then the deflection angle θ (between I and I_0 , see figure 4), is:

$$\theta \approx \lambda_0 / \Lambda \quad \dots (7)$$

A similar argument may be applied to all the higher order sidebands (figure 5) showing that all of the side bands are separated from each other by an angle θ , i.e., for a sideband of frequency $(w + Nw_s)$ where N is an integer, then the deflection from the original direction is:

$$N\theta = N \frac{\lambda_0}{\Lambda} \quad \dots (8)$$

The diffraction pattern obtained is similar to that which would be obtained from a Fraunhofer diffraction grating. Note that all the sidebands in figure 6 have their frequency Doppler shifted by the ultrasound wave by $2w_s$, $3w_s$ and etc.

The amplitude of the deflected sidebands vary according to the curves shown in figure 7. These are the Bessel functions J_0 , J_1 , J_2 etc. and when squared (figure 8) give the power or intensity of the light in each sideband. Notice that the power in each sideband varies with $\Delta\phi$, the change in phase. Thus from Equation 5 we have $\Delta\phi \propto \Delta n \propto$ changes in density. Changes in the density of the medium are equivalent to the power of the compressional acoustic wave injected into the medium.

Hence, as the power is increased, the intensity of light in the higher orders will increase. For a certain input power a phase change of 2.4 rad (or 5.3 rad etc.) will occur, causing the intensity of the zeroth order to fall to zero. Only quantized values of phase change will cause 100% deflection. Also, as the phase change increases to ∞ , the number of deflected orders generated will also approach ∞ . From figure 8, with $\phi = 2.4$ rad, the zeroth order will disappear and three sidebands will be observed on either side.

2.2.2 Limit of Debye-Sears Effect

The theory, described above, has definite upper limits, above which it does not hold. These upper limits involve interaction length L and the ultrasound frequency w_s .

Figure 9 shows adjacent portions of the acoustic column, which are alternately compressed and dilated. Each of these portions is $\Lambda/2$ high. Assume that light enters this compressed region where Δn is positive and the first order is diffracted with an angle θ . If L is long, as shown in

figure 8, then this sideband soon enters a region where n is negative. If this happens, all the sideband amplitudes fall to zero. Thus there is an upper limit for L , so that:

$$\tan \theta = \frac{\Delta/2}{L_{\max}}$$

$$\text{But } \tan \theta \approx \theta \approx \frac{\lambda}{\Delta} \quad \dots (9)$$

$$\text{or } L_{\max} = \frac{\Delta^2}{2\lambda}$$

Experiments for which this condition holds are said to lie within the Debye-Sears [2-6] or Raman-Nath [7] region. It follows from equation 9 that for a fixed L , there is an upper limit for the sound frequency for which the Debye-Sears condition is satisfied. For example, assume $f_s = 5$ MHz and $\lambda = 0.633$ micron, $L_{\max} = 3$ cm and a transducer of 1 cm square would be well within the limits. For 50 MHz in water or 300 MHz in rutile (crystalline TiO_2), a material with low acoustic attenuation even at microwave frequencies, with He-Ne light, L_{\max} is only 0.03 cm. However, we need to know what happens when L is much greater than the limit of Raman-Nath (or Debye-Sears) region.

If we split the interaction length L into a large number of short elements, δL , the first of these elements being a thin plate-like section along the left edge of the column, the phase shift $\Delta\phi$ produced is so small that only two sidebands are generated. These three waves then enter the next section where they again split, generating two new sidebands and modifying the amplitude and phase of the first two and of the carrier waves. It can be shown (see figure 10) that the amplitudes of all sidebands fall to zero after propagating through a distance L . Everywhere along the acoustic wavefront, sideband radiation is generated (dashed lines) and is deflected at an angle λ/Δ . Because of the tilt, the wavefront of sideband light produced on the left (solid tilted line) do not stay in step either with the incident light (vertical lines) or with the additional sideband light (dashed) generated further to the right. If L reaches a certain length then distinctive interference is unavoidable and all the sidebands generated cancel out. Cancellation is complete when the deflected wave has travelled a distance $2\Delta^2/\lambda$ wavelengths of light, and has passed over one whole wavelength of incident light.

This cancellation of the sidebands can also be seen for the same reason in the Raman-Nath region if the incident light is not exactly normal to the direction of the sound waves. However, if the interaction length is long (or is high), then changing the angle of incidence slightly away from the normal has a dramatic effect which will now be considered.

2.2.3 Acoustic Bragg Reflection [6,8,9]

For a long length of interaction, and/or a high acoustic frequency, and an angle of incidence of $\alpha_i = \lambda/2\Delta$, (both wavelengths measured in the medium) then the unlimited

growth of one first order sideband is seen at an angle to the incident light (see figure 11). The first upper sideband now appears to be reflected from the acoustic wavefronts as if they were mirrors and the incident light and upper first order sideband light remain in place along each acoustic wavefront, irrespective of the length L . This effect is analogous to the reflection of x-rays by crystal planes, known as Bragg-reflection and the incident angle α (Bragg angle) is equal to the reflected angle. From geometry (figure 11).

$$2\Lambda \sin \alpha = N\lambda \quad \dots (10)$$

where $N = 1$

Although N can have any integral value for crystal reflection of x-rays, but in the present case $N = 1$ is the only value that holds for acoustic Bragg reflection because of the theory of cancellation just described. This is because, in reality, the acoustic planes are not discrete planes, only a continual sinusoidal variation of the refractive index. In air the deflection angle is increased because $\lambda = \lambda_0$. Thus,

$$2\Lambda \sin \alpha = \lambda_0$$

$$\text{or } \alpha \approx \frac{\lambda_0}{2\Lambda} \quad (\text{for small } \alpha \text{ in air}) \quad \dots (11)$$

It should be noted that this cumulative interaction occurs only for one first order sideband; the other one and all the other higher-order sidebands are still subject to destructive interference. This striking phenomenon, which permits the unlimited growth of one first-order sideband, is called Acoustic Bragg Reflection, in analogy to the selective reflection of X-rays by the lattice plane of the crystals. The angle $\sin \alpha \approx \lambda_0/2\Lambda$ - more precisely $\sin \alpha = \lambda_0/2\Lambda$, is called the Bragg angle.

It may be shown [6] that the amplitude of the sideband or diffracted wave first increasing linearly with $\Delta\phi$, become equal to the full carrier amplitude when $\Delta\phi = \pi$, and at that point the incident light is completely suppressed. The carrier wave amplitude is also completely suppressed at 3, 5, 7 and etc. radians (figure 12).

The behaviour of the amplitudes of incident and diffracted light resembles that of the voltages on two symmetrical, loosely coupled transmission lines. We may think of the four plane waves of light, travelling under the positive and negative Bragg angle with respect to the acoustic wavefronts. The frequency shift from one to the other does not fit transmission-line analogy. It can be interpreted as a Doppler shift. It is positive or negative, depending on whether the incident light wave is directed to meet the sound wave or to catch up with it (figure 13). In the first case, the upper first order side band is produced and in the second case the lower one is evidenced. The option of selecting a single sideband by merely changing orientation is a valuable feature of Bragg reflection. A single mode of diffracted light is produced, whose

frequency is upshifted or downshifted as desired and whose amplitude is a sinusoidal function of sound amplitude and interaction length. Complete conversion occurs when the cumulative phase excursion equals π and odd multiples of π .

2.2.4 The Factor Q

A factor Q may be defined [10] which, for a given system, will tell us if that system is operating in the Debye-Sears region or in the Bragg region.

$$Q = \frac{2\pi L \Delta}{2} = \frac{2\pi L \Delta_0}{n \Lambda^2} \quad \dots 11)$$

Equation 11 summarizes the dependence of a system on L and Λ^2 as all the other parameters are constant for a given system. The single most important objective in both types of diffraction is to be able to deflect 100% of the light away from the zeroth order (i.e. $I_0 \approx 0\%$).

Debye-Sears Region

- (i) The incident angle must be normal to the direction of the propagation of sound waves.
- (ii) $Q \ll 1$ (i.e. $Q < 0.1$)
- (iii) The minimum acoustic power must be such that it produces a maximum phase change $\Delta\phi$ which is equal to 2.4 radians.

Bragg Reflection Region

- (i) The incident angle must be Bragg angle, $\alpha \approx \lambda_0/2\Lambda$.
- (ii) $Q \gg 1$ (i.e. $Q > 10$), see figure 14.
- (iii) The minimum acoustic power must be such that it produces a maximum phase change, $\Delta\phi = \pi$ radians.

The Transition Region

- (i) $Q \approx 1$

In this region 100% deflection is possible only at the incident Bragg angle, but the minimum phase change must be higher than π radians (see figures 15 and 16).

2.2.6 Power Considerations

To obtain 100% deflection, the plane compressional travelling wave must cause variations in density leading to sinusoidal variations in the refractive index resulting in minimum phase changes of at least 2.4 radians for the Debye-Sears region or π radians for the Bragg region. A minimum acoustic power for both regions may be calculated thus.

The refractive index change Δn is related to the strain in the following manner [11].

$$\Delta n = \frac{n^3 P}{2} s \quad \dots (12)$$

where P is the photoelastic constant of the medium. Note that an increase in n produces a compression, i.e. a negative strain.

The strain is related to the acoustic intensity I by [9].

$$s = \frac{(2I_{ac})}{(\rho v_s^3)} \quad \dots (13)$$

where ρ is the density of the medium (kg/m^3) and v_s the velocity of sound in the medium.

Now from equation 5, we have:

$$\begin{aligned} \Delta \phi &= \frac{2\pi L}{\lambda_0} \Delta n \\ &= \frac{2\pi L}{\lambda_0} \frac{n^3 P}{2} \frac{(2I_{ac})}{(\rho v_s^3)} \quad \dots (14) \end{aligned}$$

$$= \frac{\pi L}{\sqrt{2} \lambda_0} \frac{(n^6 P^2 I_{ac})}{(\rho v_s^3)}$$

A figure of merit factor M may be defined,

$$M = \frac{n^6 P^2}{\rho v_s^3} \quad \dots (15)$$

Thus, from equation 14, we get

$$\Delta \phi = \frac{\pi L}{\lambda_0 \sqrt{2}} (M I_{ac})^{1/2}$$

Hence, the minimum acoustic power required for 100% deflection for Debye-Sears (or Raman-Nath) region for the condition that $\Delta \phi = 2.4$ radians, is

$$I_{ac} = \frac{(2.4 \lambda_0 \sqrt{2})}{(\pi L)} \frac{1}{M} \text{ W/m}^2 \quad \dots (17)$$

Similarly, the minimum acoustic power required for 100% deflection in the Bragg region when we need $\phi = \pi$, is

$$I_{ac} = \left(\lambda_0 \frac{\sqrt{2}}{L} \right)^2 \frac{1}{M} \quad \dots (18)$$

The more generalised result for the deflected power under Bragg condition is [11].

$$\frac{I_{\text{diffracted}}}{I_{\text{incident}}} = \sin^2 \left| \frac{\pi L}{\lambda_0 \sqrt{2}} (M I_{RC})^{1/2} \right| \quad \dots (19)$$

The squared Bessel function (figure 8) is equivalent to this for Debye-Sears region but clearly cannot be expressed in as simple a form as equation 19.

Let us consider water as an example of an acousto-optic medium in which sinusoidal acoustic plane wave is delivered using the following values, $n = 1.33$, $P=0.31$, $\rho=1000 \text{ Kg/m}^3$ and $V_s = 1500\text{m/s}$, we get from equation 15:

$$M = 1.57 \times 10^{-18} \text{ s/g}$$

For a coherent light source of wavelength = 0.6328 microns (He-Ne), acoustic power required for Debye-Sears 100% deflection (from equation 17), for an interaction region $10\text{cm} \times 1\text{cm}$, ($L=10\text{cm}$), is

$$I_{ac} = 0.3\text{W}$$

Similarly for Bragg reflection of 100%, for the same cell area, from equation 18, is

$$I_{ac} = 0.5 \text{ Watt}$$

2.3 Acousto-Optic Materials

The figure of merit, M , for a material (equations 17 and 18), is

$$I_{ac} \propto \frac{1}{M}$$

$$\text{where } M = \frac{n^6 P^2}{\rho V_s^3} \quad (\text{see equation 15})$$

All four parameters n , P , ρ and V_s for the expression for M are properties of the material in which the interaction takes place. By far, the greatest variation is caused by the refractive index n and the photoelastic constant P which is defined as the derivative of the reciprocal of the refractive index ϵ_0/ϵ (for optical frequencies) with respect to S . These two latter parameters should be as high as possible to ensure a high value for M and V should be as low as possible for the same reason. Liquids generally have lower densities and lower acoustic velocities than crystals and glasses. It may be noted from equation 6, that the diffraction angle,

$$\theta = \frac{\Delta \lambda_0}{\lambda_0} = \frac{\Delta \lambda_0 f_s}{V_s}$$

or $\propto \frac{1}{V_s}$... (21)

Hence low acoustic velocity provides both high figure of merit and large deflection angle. Liquids, with their low sound velocities have higher M values than solids and the best solids are those (glasses and crystals) which have high refractive indices. It should also be noted that liquids may not be quite suitable at higher frequencies because of their excessive attenuation of ultrasound. For example, in materials, such as water ($V = 1500\text{m/s}$) the acoustic attenuation is very high at $2.4 \times 10^{-3} \text{ dB/cm/MHz}$ at 1 MHz, increasing with the square of frequency. At 50 MHz the acoustic attenuation at room

temperature is about 6 dB/cm. This severely restricts its use at higher frequencies. Acoustic attenuation is much smaller in solids and increases more slowly with frequency. Quartz, Rutile, Sapphire and Lithium Niobate have very low acoustic attenuation and fairly good values of figure of merit M . Amongst the liquids water has the lowest acoustic attenuation coefficient. Table 1 gives an approximate comparison of relevant parameters for materials for acousto-optic devices. For the present application, Water and TeO_2 (used in its slow shear mode [110]), seem ideal materials for acousto-optic device with a large deflection angle. However, if cost is an important criterion, water must be seriously considered, because its performance in terms of M and acoustic attenuation is not all that different from TeO_2 .

2.4 Present State of Progress made with Contract No. DAJA45-83-C-0016

2.4.1 Introduction

Experiments were performed by directing a He-Ne laser at various angles of incidence, into an ultrasound beam in a brine filled acousto-optic cell. The ultrasound was fed into the brine cell through a polyvinylidene fluoride (PVDF) transducer. PVDF (fig. 17) was chosen because its acoustic impedance (2.3 Rayls) is comparable to that of water (1.48 Rayls) and it provides a good acoustic match. The acoustic impedance of ceramic piezoelectric transducers is approximately an order of magnitude higher than that of PVDF.

The acoustic impedance Z may be defined as the product of acoustic velocity and the density of the material.

$$Z = \rho v_s \quad \dots (22)$$

When an a.c. field of sufficient magnitude is applied to the electrodes of a piezoelectric device, it begins to vibrate. The acoustic power is emitted from either side but will tend to propagate in the direction that has the superior acoustic match. The front end must therefore be very well matched and back end or backing material must be badly matched. If the acoustic impedance of the front and back are normalized to that of the transducer, then the ratio of the power delivered in the forward direction will be the ratio of the normalised front and back impedances. PVDF has also a low value of quality factor (QF) of 3 which provides a wide bandwidth. The films in PVDF can be made very thin which produces thickness mode resonances in the megahertz (MHz) region. However, above 1 MHz the material becomes lossy and at 20 MHz PVDF has α_a -relaxation which makes its usefulness rather restricted. Assuming perfect operation of PVDF transducer only 10% of the input power is converted into mechanical perturbation. If the power amplifier following the PVDF transducer is well matched, then it is estimated that the minimum power required for 100% deflection in the Debye-Sears region (assuming 5% efficiency) is approximately 6 watts. Obviously in the practical case more power will be required for 100% deflection in both Debye-Sears and Bragg modes of operations.

2.4.2 PVDF Transducer with Brine Filled Acousto-Optic Cell

Figure 17 shows schematically the acousto-optical cell which was made of perspex with small glass windows on either side and a thick angled acoustic absorber placed at the back of the cell to absorb most of the forward wave (figure 18). The acoustic channel was designed to be exactly the size of the transducer electrode leaving 2mm gap all round the sides. The inside walls of channel are totally smooth so there will be no corruption of the forward plane waves. The cell was filled with 1 mol solution of brine which, being an electrolyte, became the front electrode. The brine is now in direct contact with the PVDF and act as an effective coolant as well. Brine being slightly denser, provides also a better acoustic match to PVDF which is not attached by it. Figure 18 shows the schematic arrangement of the transducer assembly in which 150 μm thick pre-stretched and pre-poled PVDF is glued to a PCB using Araldite at 70°C and 6 tons of pressure for 12 hours. The complete experimental arrangement is shown schematically in figure 18 which is self-explanatory. By far the most reliable way of recording qualitative results over a large frequency range, incident angle and input power, was by photographically recording the diffraction pattern obtained. This was done by placing the camera, without a lens in the path of the diffracted beam and using an exposure time of 1/1000th of a second and Ilford FP4 films. For a quantitative measure of intensities of the diffracted beams solid state photodetectors were used at appropriate locations.

2.4.3 Results and Discussion (Acousto-Optic Brine Cell & PVDF Transducer)

The frequency of the acoustic wave was increased from 1 MHz to 20 MHz and the angle of acousto-optic deflection was observed to increase linearly as expected, the angle of deflection being approximately 1° which is in agreement with the theory. Figures 19 and 20 show the behaviour of the deflection angle with respect to frequency for both the Debye-Sear mode (normal incidence) and the Bragg mode (oblique incidence) respectively. When the laser beam is incident normal to the cell (Debye-Sears type of diffraction) up to three diffracted spots of light are seen on either side of the zeroth order beam at frequencies less than 15 MHz. When the laser beam is incident only at the Bragg angle (Bragg type of diffraction) only one diffracted spot is visible and its angle away from the zeroth order is observed to be twice that for the first order spot in the normal incidence case. This single spot was not found to be visible at very low frequencies, (i.e. less than 2 MHz), but remained visible as the frequency was increased up to 40 MHz. Thus the Debye-Sears diffraction is dominant for lower frequencies and at higher frequencies Bragg-diffraction is effective. Between 3 MHz and 15 MHz the experimental results suggest that the system operates in the transition-region.

Figure 21 shows the percentage of deflected power as a function of ultrasound frequency for the two mechanisms, described above. It may be observed (figure 21) that for normal incidence (Debye-Sears diffraction) at 3.5 MHz ultrasound frequency, 100% deflection of incident energy is achieved. This observation is further supported by photographic recording of the results (figure 22). For 100% deflection at 3.5 MHz the incident acoustic power output from the power amplifier was 8W in contrast to the expected value of 0.3W for the Debye-Sears region. Thus the overall efficiency of the system is approximately 3.7%. This is, however, not far from the theoretically expected value of 5% maximum efficiency. In contrast, at 20 MHz, in the Bragg region, the net electrical power output from the amplifier was 28W and yet only 12% of the laser power is deflected and the overall efficiency of the system in the latter case is only about 0.2%.

Above results show that water (Brine) is an excellent low frequency acousto-optic medium because of its acoustic properties. Its low acoustic velocity gives rise to larger deflection angles than other acousto-optic materials. It could also be operated in the Bragg region as a deflector. However, to achieve the Bragg reflective condition with water, a long interaction length (~10cm) and a high ultrasound frequency (15 MHz) are needed to satisfy the condition $Q \gg 10$. If the system were electrically matched at 15 MHz, it should be possible to deflect most of the incident laser light because of the high input power available at this frequency. However, it would operate relatively inefficiently due to the high dielectric loss.

Present work has shown clearly that using Brine as the acousto-optic interaction medium it is possible to deflect He-Ne laser ($\lambda = 0.6328$ microns) in which 100% of the energy in the zeroth order beam is transmitted to higher orders in the Debye-Sears region.

2.4.4 Detection of Coherence by Acousto-Optic Interaction

A permanently activated acousto-optic cell may only be useful if it deflects coherent radiation without affecting non-coherent radiation, i.e. if the aperture is useful for viewing when the cell is activated. In order to test this facility a 5 mW laser and light from a quartz halogen lamp (white light) were both incident on a PVDF actuated cell in the same plane. The incoherent source was made narrow and parallel by a converging lens arrangement. The white light source was made monochromatic by the use of filters (red, yellow or blue) and the filtered spot and the laser spot were incident side by side on a white sheet of paper. When the acousto-optical cell was energised the laser spot was split into three orders of deflection on either side of the zeroth order primary beam. The energy shift was greater than 84%. No deflection of the incoherent beam could be detected for any of the filter colours.

The lack of deflection of the coherent beam was further demonstrated by inserting a coloured photographic transparency in the optical path and re-assembling the image on the far side of the cell. When the acousto-optic

cell was inactive the first print of the transparency could be clearly made out in the transmitted image. When the cell was activated with 6 watts of acoustic power, there was no difference in the clarity of the image of the transparency. This clearly demonstrated that the acousto-optic cell would have no adverse effect on incoherent radiation which can be employed for normal viewing purposes whilst the coherent laser beam being sensitive to diffraction effects.

2.4.5 Tellurium Dioxide (TeO_2) Cell

A wide aperture TeO_2 crystal of high optical quality and low distortion replaced the water cell of the previous work. The cell was provided by Crystal Technology Inc., Palo Alto., Ca, USA. TeO_2 crystal was used in the shear mode with carefully matched transducers. The estimated energy in the deflected beam using a system shown in figure 23 was approximately 84%.

In figure 23 the first lens converges the essentially parallel rays to a point located in the deflector system. High efficiency TeO_2 with acoustic velocity 4260 m/s interacts with the coherent laser beam to produce nearly 100% deflection at 100 MHz. The beam separation under these conditions is 15 milli-radians. The remainder of the optical components consists of lenses to reinvert the image and to bring out the beam as parallel rays. A complete system, described above and operating at 80 MHz, was in November 1986 which has demonstrated this principle of efficient deflection of coherent He-Ne laser beam ($\lambda = 0.633$ microns) satisfactorily, although the TeO_2 crystal by then, had developed a serious crack which reduced the deflection efficiency from 84% to approximately 50%.

2.4.6 Summary

Present work has shown that 100% of incident energy of a coherent laser beam of 5 mW power and $0.63 \mu\text{m}$ wavelength can be deflected by acousto-optical interaction energy at 3.5 MHz at an angle 1 degree from the original direction of incidence using PVDF transducer and water cell as the interacting medium.

PVDF transducer and the water cell were replaced by a single crystal of Tellurium dioxide as a single integrated detector-deflector system. The estimated energy of the deflected beam was approximately 84% of the incident radiation, the deflection angle being $\sim 3^\circ$ at 84 MHz.

An alternative method of transferring most of the energy of the incident radiations through large deflecting angle (18 degrees or more) is to use appropriately blazed diffraction (transmission type) gratings and further work is necessary in this project.

References

1. L. Brillouin, Ann. Phys. (Paris), 9th Ser. 17, 88 (1922).
2. P. Debye & F.W. Sears, Proc. Nat'l Acad. Sci (USA), 18, 409 (1932).
3. R. Lucas & P. Biquard, J. Phys. Rad., 7th Ser., 3, 464 (1932).
4. L. Ali, Helv. Phys. Acta, 8 503 (1935).
5. L. Ali, Helv. Phys. Acta, 9, 63 (1936).
6. R. Adler, IEEE Spectrum, 42, May (1967).
7. C.V. Raman & N.S.N. Nath, Proc. Ind. Acad. Sci., 2A, 413 (1935).
8. H.Z. Cummins & N. Knable, Proc. IEEE (Correspondence) 51, 1246, Sept. (1963).
9. C.F. Quate, C.D.W. Wilkinson and D.K. Winslow, Proc. IEEE, 53, 1604 (1965).
10. W.R. Klein & W.D. Cook, IEEE Trans. Sonics & Ultrasonics, S-U14, No.3, 123 (1967).
11. Y. Yariv, "Introduction to Optical Electronics", Second Ed, Holt, Rinehart & Winston, Chapter 12, p. 346 (1976).

Table 1: Properties of various acousto-optic media typically employed devices.

Units	Range of Transparency	Density	Acoustic Velocity	Refractive Index	Photo-elastic Constant	Figure of Merit	Acoustic Attenuation at 1 MHz	Max acoustic frequency possible
Symbol	—	ρ	V_s	n	P	$\frac{s^2}{g}$	$\frac{dB}{cm/MHz}$	f_{max}
Material	—	Kg/m^3	m/s	—	—	$\times 10^{-10}$	$\times 10^3$	MHz
Water	0.2 — 0.9	997	1490	1.33	0.31	156	2400	300
Fused Quartz	0.2 — 4.5	2200	5900	1.46	0.2	23.9	12	500
TeO ₂ Slow Shear	0.35 — 5.0	6000	616	2.6	0.09	793	290	148
TeO ₂ Longitudinal	0.35 — 5.0	6000	4200	2.6	—	34.5	6.3	~500
Pb ₂ MoO ₆	0.4 — 5.0	7100	2900	2.18	—	127	25	~500
LiTaO ₃	0.4 — 5.0	7450	6190	2.18	—	1.37	0.062	~2000
Lithium Niobate	0.4 — 5.0	4640	6570	2.20	0.15	7.0	0.098	~2000

Figure Legends

- Table 1. Properties of various acousto-optic media typically employed in devices.
- Figure 1. The basic Acousto-optic device.
- Figure 2. Optical Delay Line. Variation of refractive index n produces phase modulation.
- Figure 3. Sinusoidal compression wave giving rise to spatial variation of the density and hence index of refraction.
- Figure 5. Sound wave travelling upward generates sinusoidal variation of refractive index, generating optical phase shifts, which combine to tilt the wavefront of the first-order upper sideband. Carrier wavefront remains unaltered.
- Figure 6 The Debye-Sears Effect
- Figure 7 Carrier and sideband amplitudes of a phase modulated wave versus phase excursion, $\Delta\phi$. These curves are Bessel functions J_0, J_1, J_2, J_3 , etc.
- Figure 8 Light intensities in the sideband amplitudes of a phase modulated wave versus phase excursion, $\Delta\phi$, i.e. Bessel functions squared.
- Figure 9 The critical length. Light starting in compressed portions of the sound wave spreads by diffractions into dilated portions. The value L_{max} is the upper limit of the Debye-Sears regime.
- Figure 10 Destructive Interference. Contributions to the sideband generated at different points along the acoustic wavefront (dashed lines) do not add up in phase.
- Figure 11 Bragg Reflection. Constructive interference leads to a build up of one selected first-order sideband. Horizontal lines are acoustic wavefronts; tilted lines, wavefronts of incident and diffracted light.
- Figure 12 Zeroth and first order light intensities versus the phase change $\Delta\phi$ with $Q \rightarrow \infty$ and light incident at the Bragg angle.
- Figure 13 Bragg reflection. Upper or lower sideband is selected by making light and sound meet under the appropriate angle.
- Figure 14 Zeroth and first order light intensities versus Q with the phase change $\Delta\phi = \pi$ radians and light incident at the Bragg angle.
- Figure 15 The Transition Region. Zeroth and first order light intensities versus the phase change $\Delta\phi$ at normal incidence with $Q=4$. al. [5].

- Figure 16 The Transition Region. Zeroth and first order light intensities versus the phase change ϕ at Bragg incidence with $Q=4$.
- Figure 17 Brine filled acousto-optic cell. Note acoustic channel is same height as transducer and the back consists of a thick angled perspex absorber.
- Figure 18 Block diagram of the general equipment layout.
- Figure 19 Deflection angle as a function of frequency. Laser at normal incidence.
- Figure 20 Deflection angle as a function of frequency. Laser incident at the Bragg angle.
- Figure 21 Deflected power as a function of sound frequency for light incident at normal and Bragg incidence.
- Figure 22 Series of photographs of diffraction pattern for various sound frequencies. Light at normal incidence.
- Figure 23 Integrated detector/deflector system.

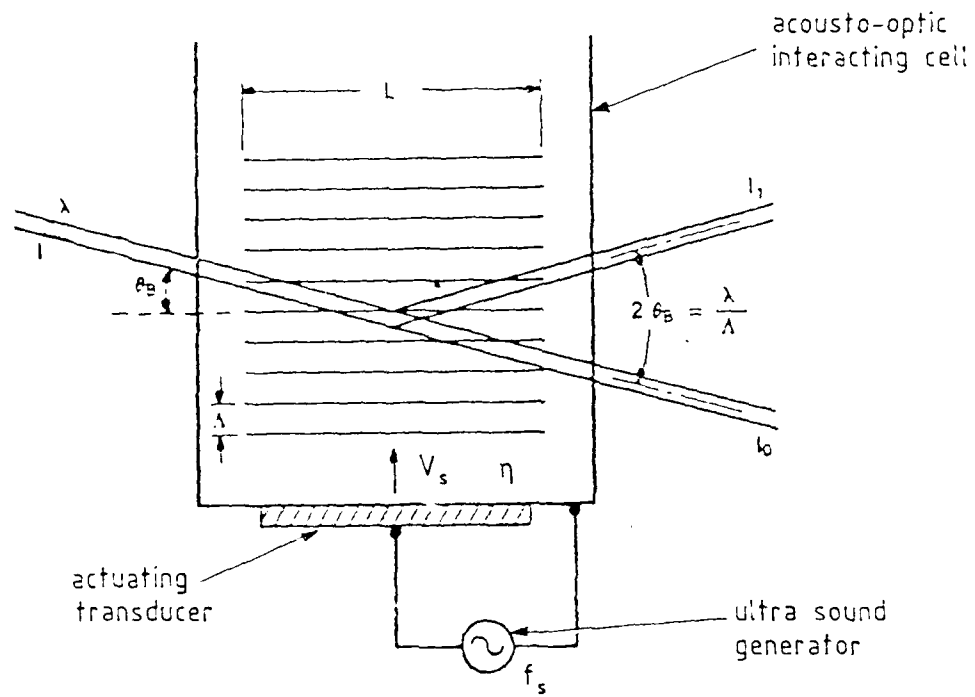


Figure 1. The basic acousto-optic device.

λ = wavelength of coherent radiations

Λ = wavelength of ultrasound waves

L = acousto optic interaction length

η = refractive index of interacting cell median

V_s = velocity of ultrasound in the cell median

f_s = frequency of ultrasound

I = intensity of coherent beam

Figure 2. Optical Delay Line. Variation of refractive index n produces phase modulation.

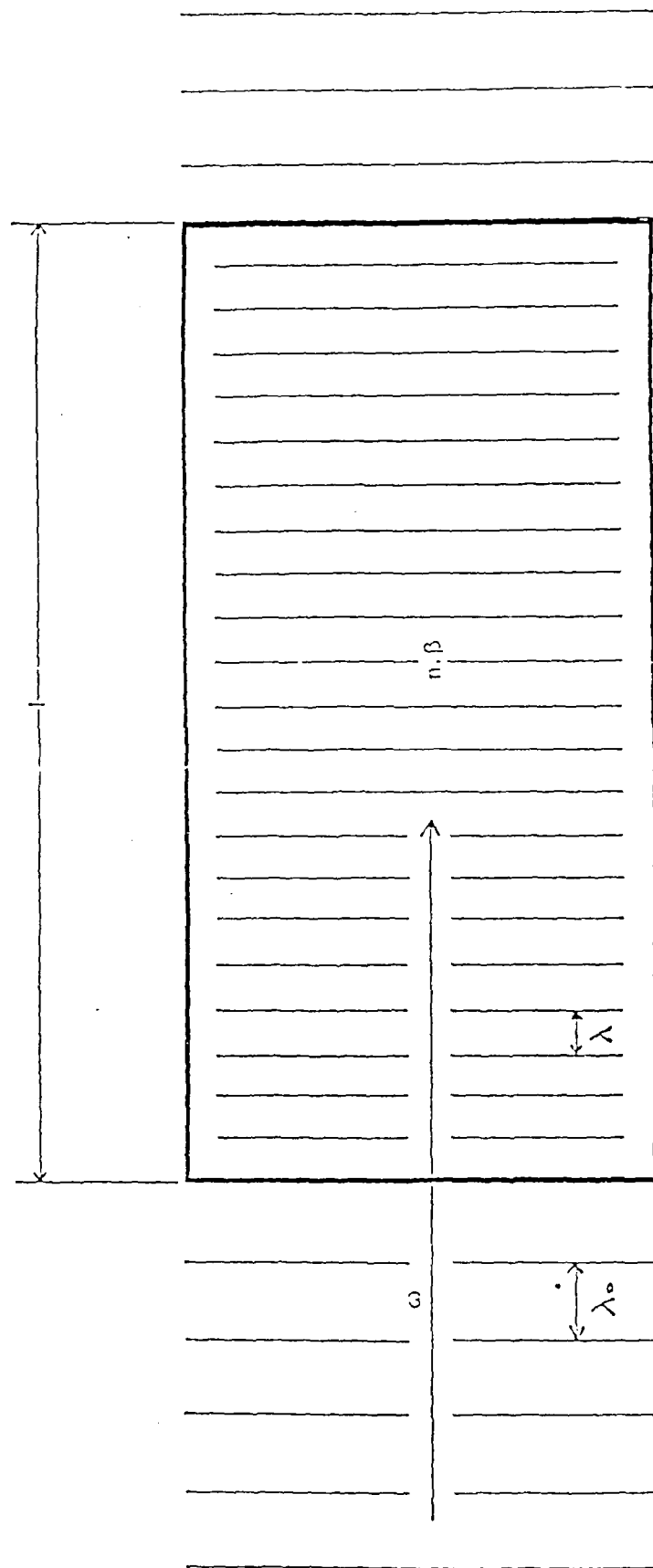


Figure 3. Sinusoidal compression wave giving rise to spatial variation of the density and hence index of refraction.

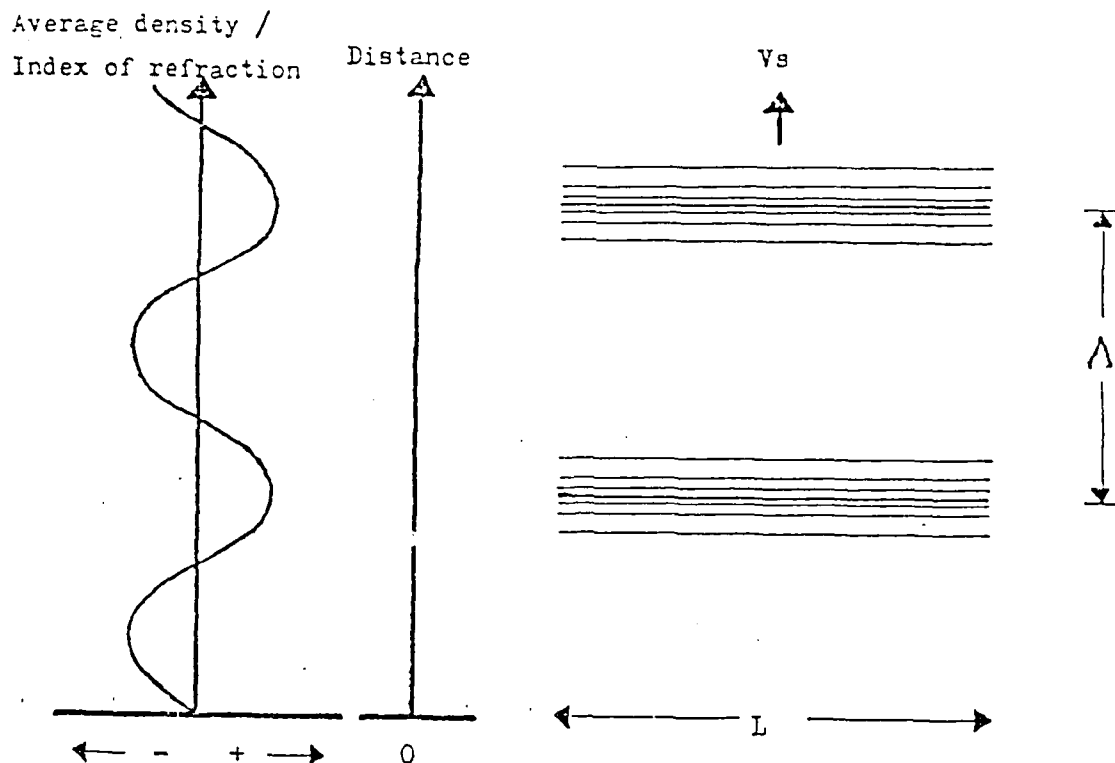


Figure 4. Carrier and Sideband Spectrum of a typical phase modulated wave.

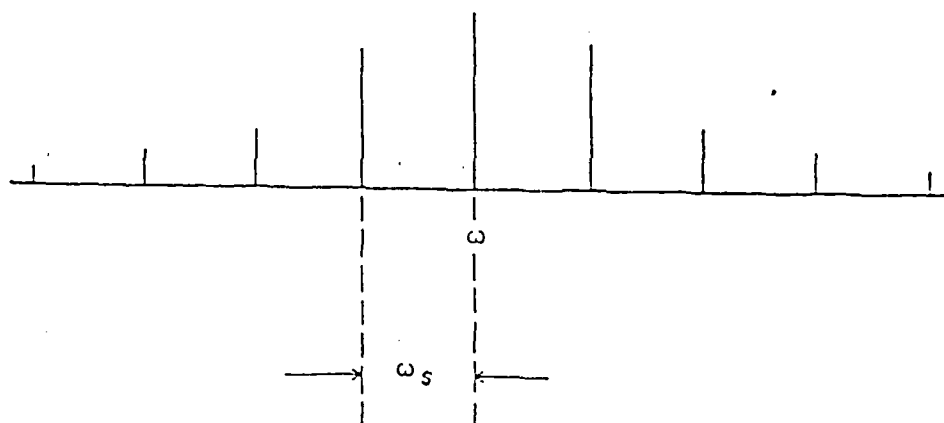
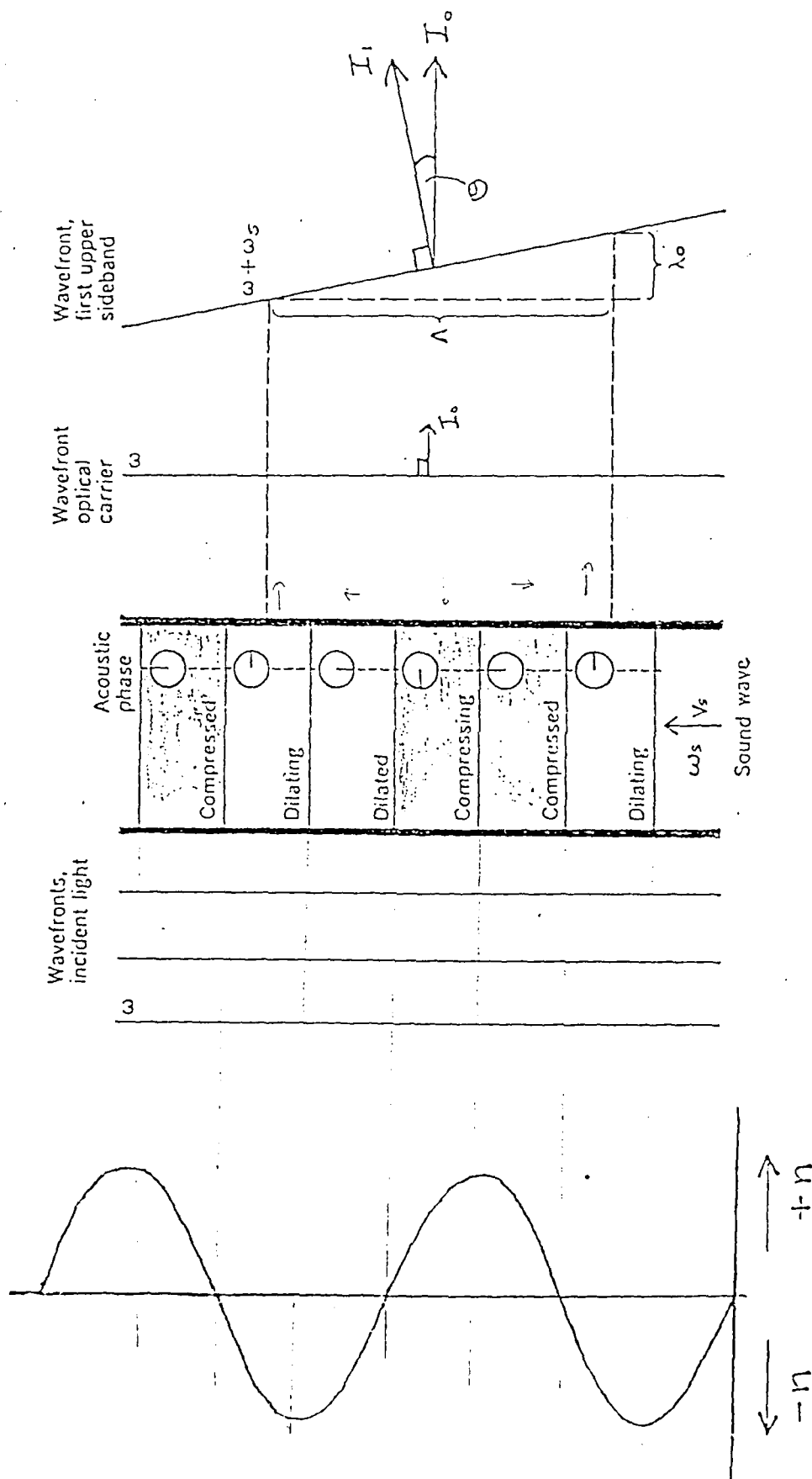


Figure 5. Sound wave travelling upward generates sinusoidal variation of refractive index, generating optical phase shifts, which combine to tilt the wavefront of the first-order upper sideband. Carrier wavefront remains unaltered.



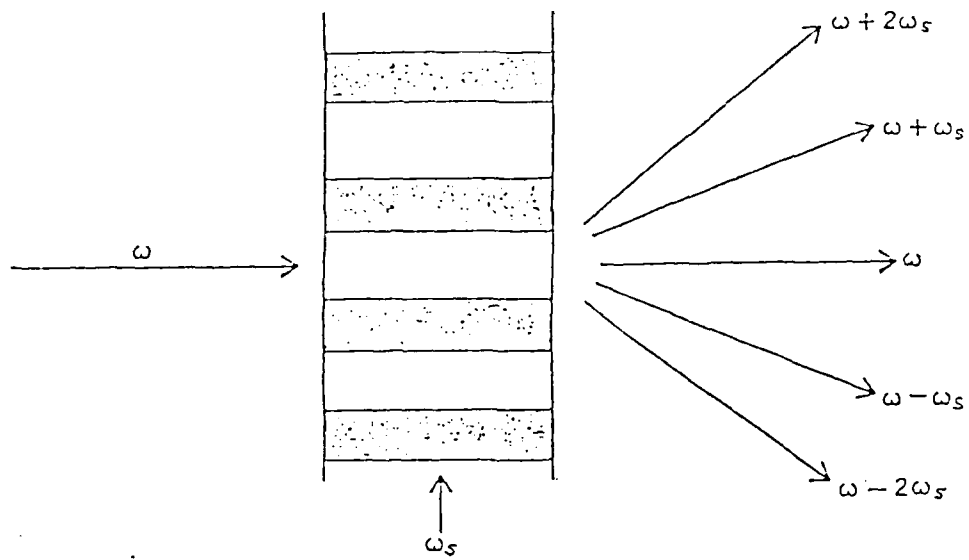


Figure 6. The Debye-Sears Effect.

Figure 7. Carrier and sideband amplitudes of a phase modulated wave versus phase excursion, $\Delta\phi$. These curves are Bessel functions J_0 , J_1 , J_2 etc.

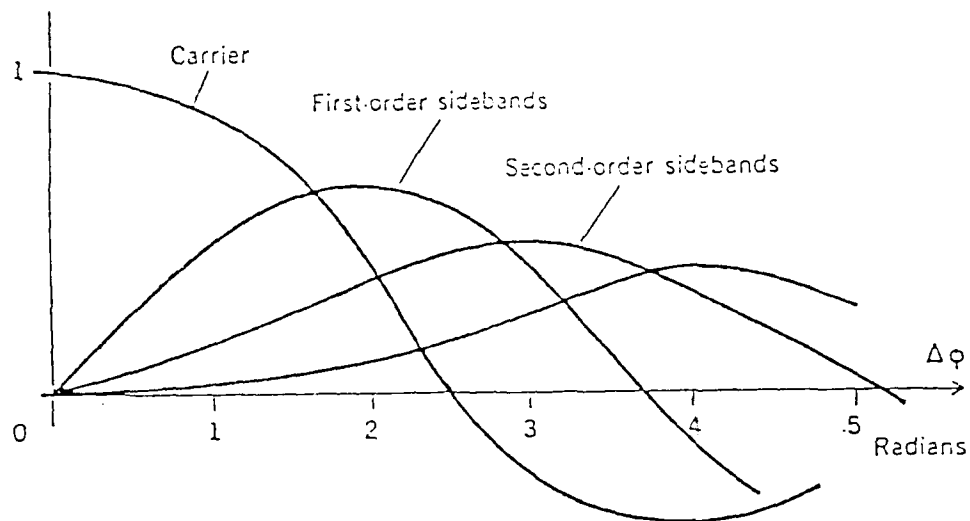
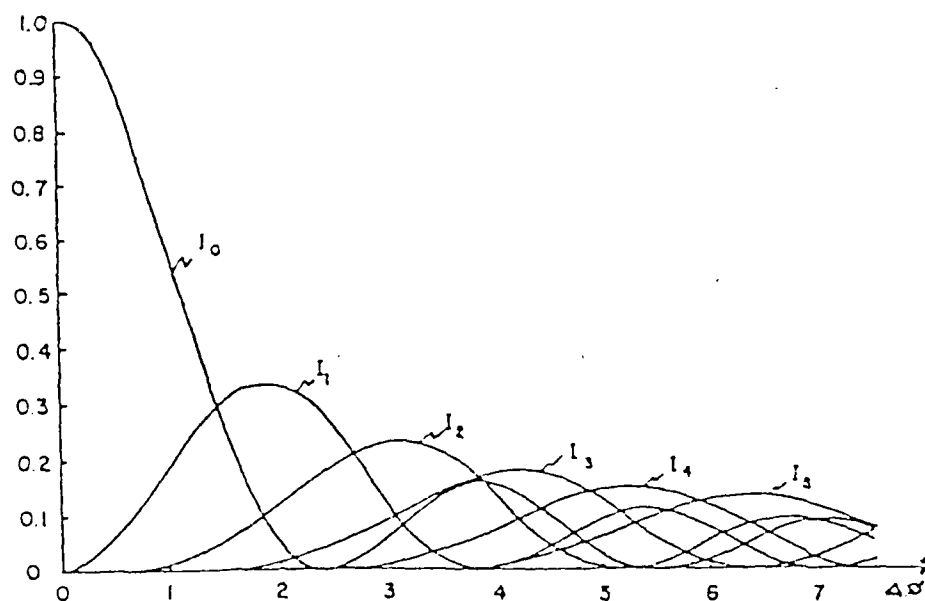


Figure 8. Light Intensities in the sideband amplitudes of a phase modulated wave versus phase excursion, $\Delta\phi$, i.e. Bessel functions squared.



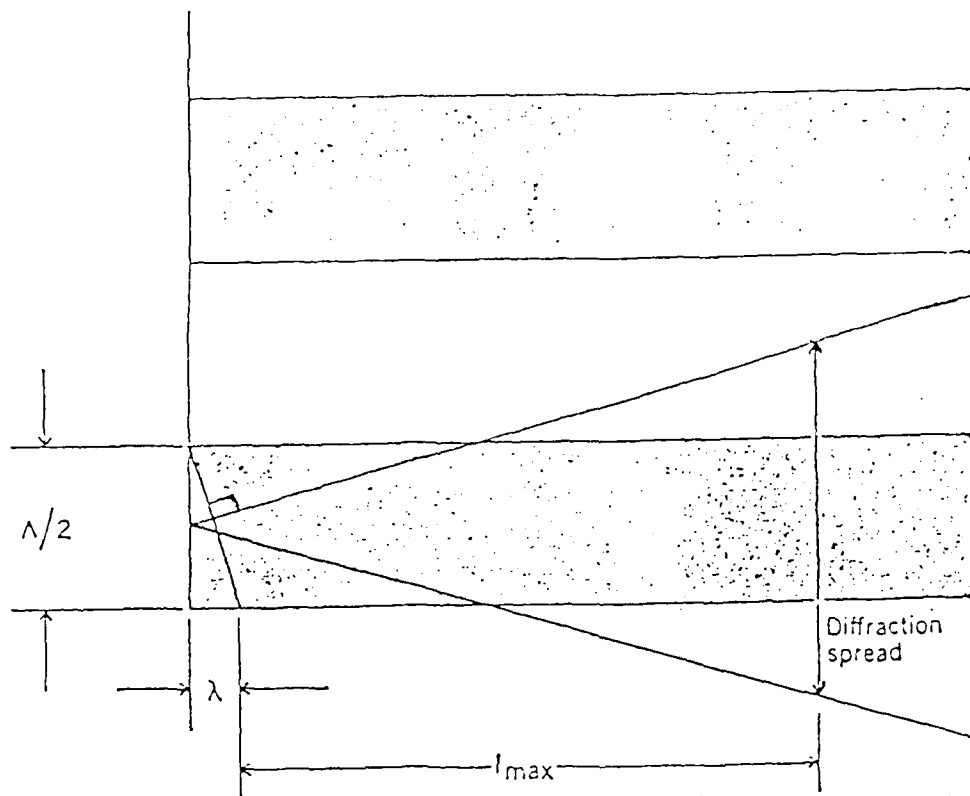


Figure 9. The critical length. Light starting in compressed portions of the sound wave spreads by diffractions into dilated portions. The value l_{max} is the upper limit of the Debye-Sears regime.

Figure 10. Destructive Interference. Contributions to the sideband generated at different points along the acoustic wavefront (dashed lines) do not add up in phase.

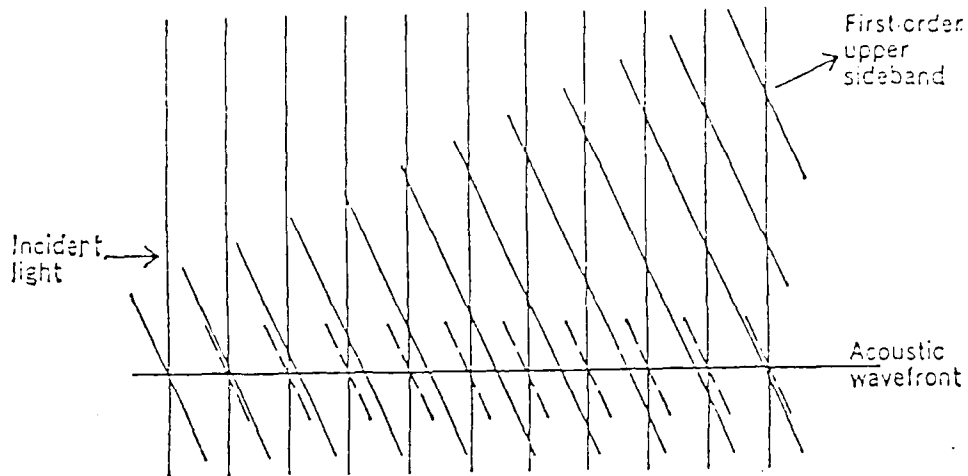


Figure 11. Bragg Reflection. Constructive interference leads to a build up of one selected first-order sideband. Horizontal lines are acoustic wavefronts; tilted lines, wavefronts of incident and diffracted light.

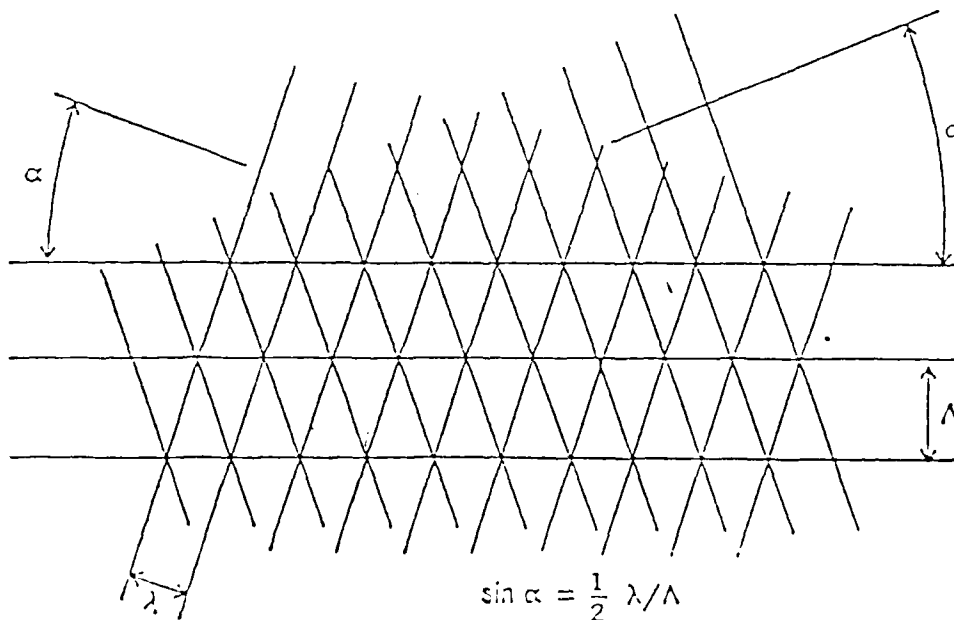
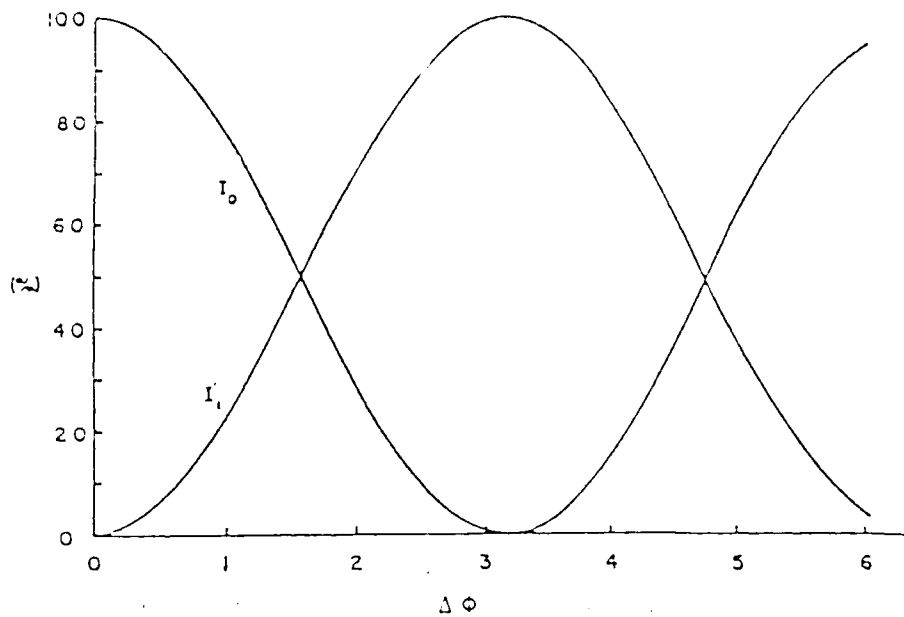


Figure 12. Zeroth and first order light intensities versus the phase change $\Delta\phi$ with $Q = \pi$ and light incident at the Bragg angle.



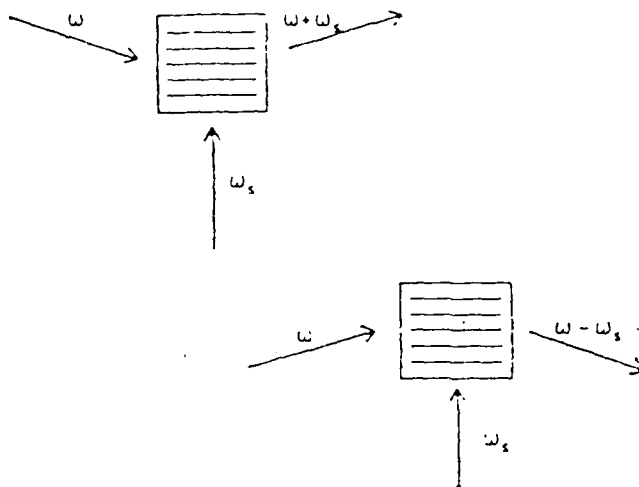


Figure 13. Bragg reflection. Upper or lower sideband is selected by making light and sound meet under the appropriate angle.

Figure 11. Zeroth and first order light intensities versus Q with the phase change $\Delta\phi = \pi$ radians and light incident at the Bragg angle.

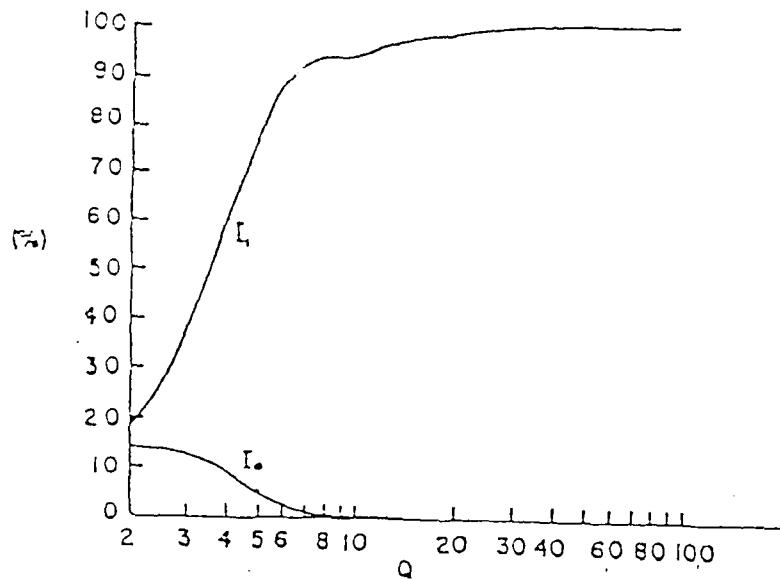


Figure 15. The Transition Region. Zeroth and first order light intensities versus the phase change $\Delta\phi$ at normal incidence with $Q=4$. al.[5].

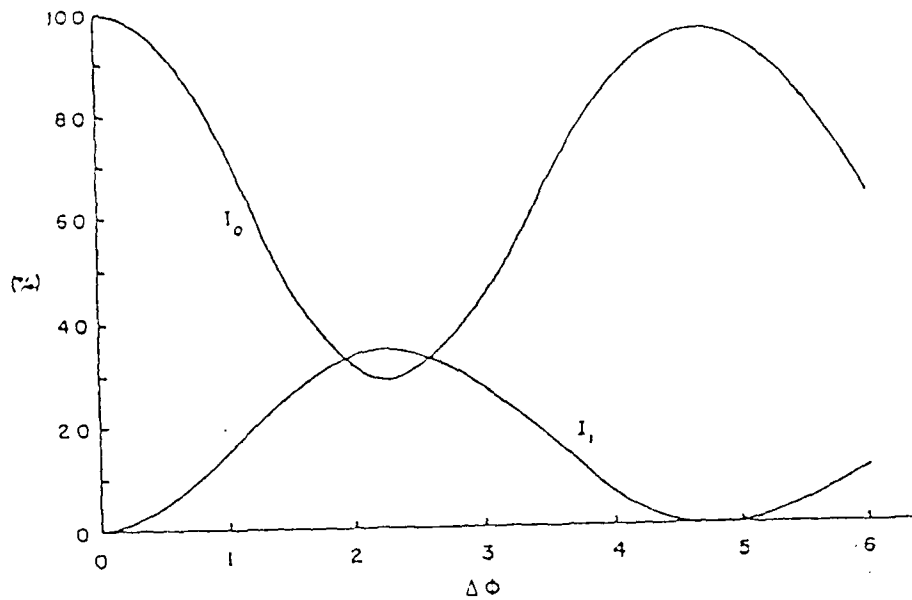


Figure 16. The Transition Region. Zeroth and first order light intensities versus the phase change $\Delta\phi$ at Bragg incidence with $Q=4$.

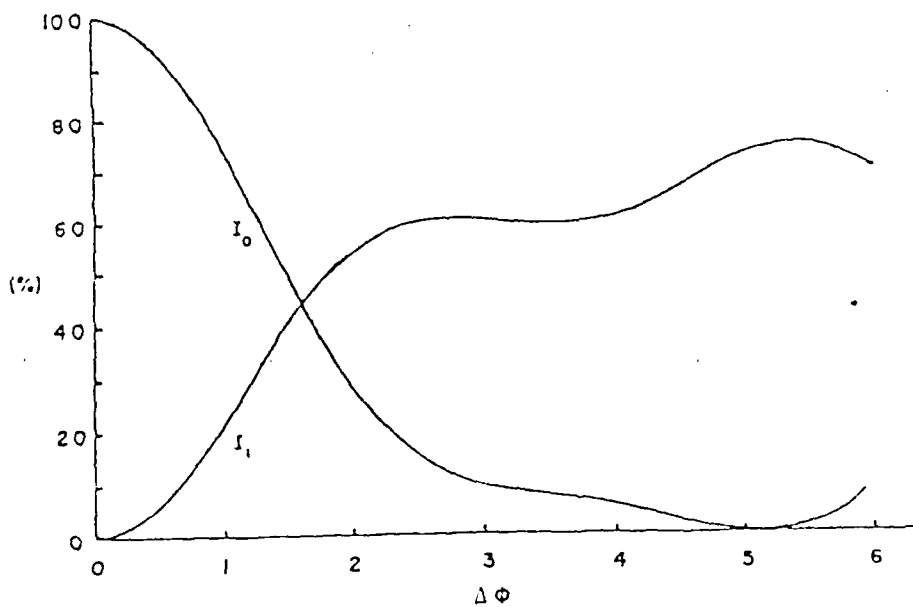


Figure 17. New brine filled acousto-optic cell.
The acoustic channel is same height as transducer and
the back consists of a thick angled perspex absorber.

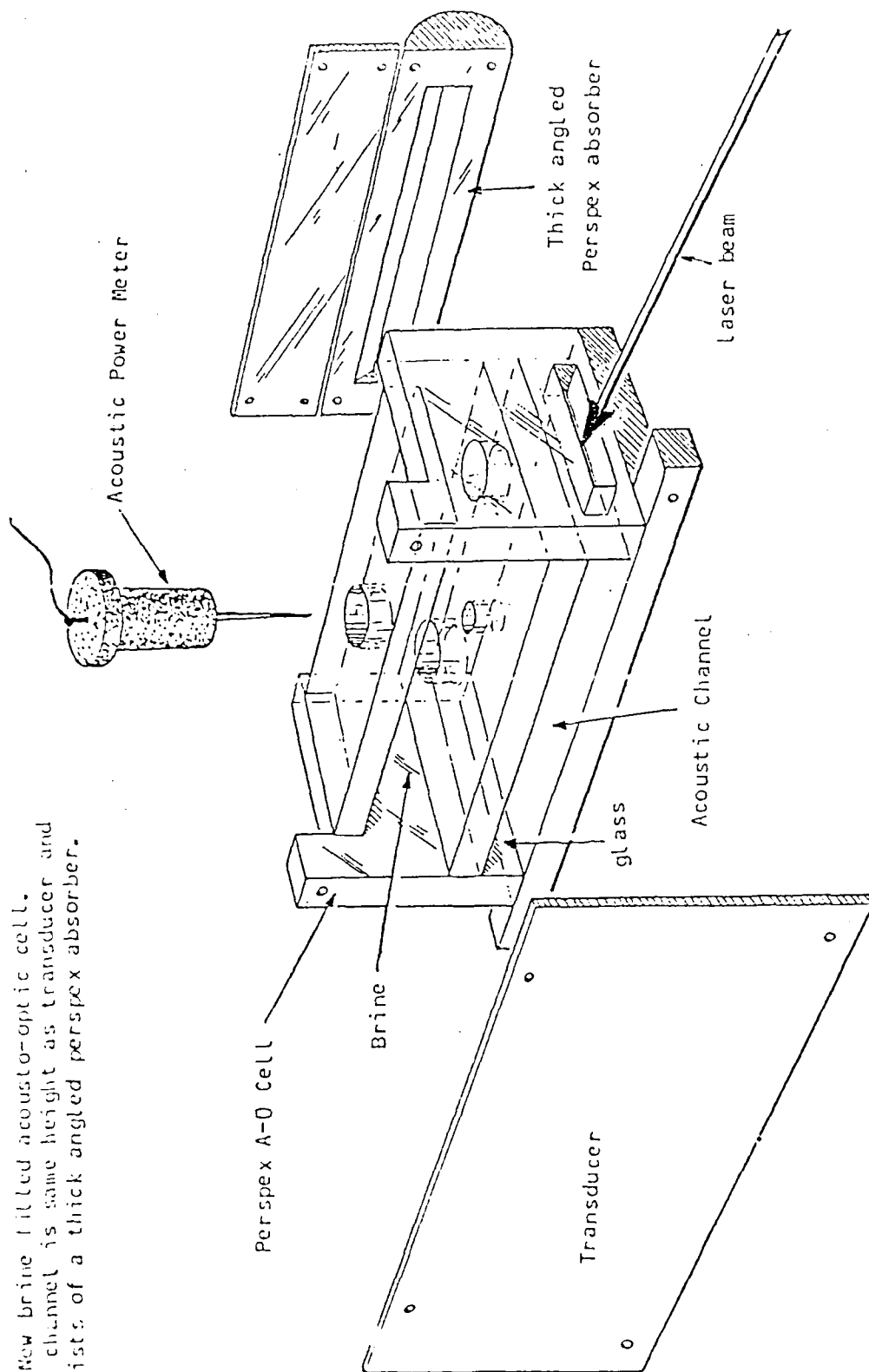


Figure 18. Block diagram of the general equipment layout.

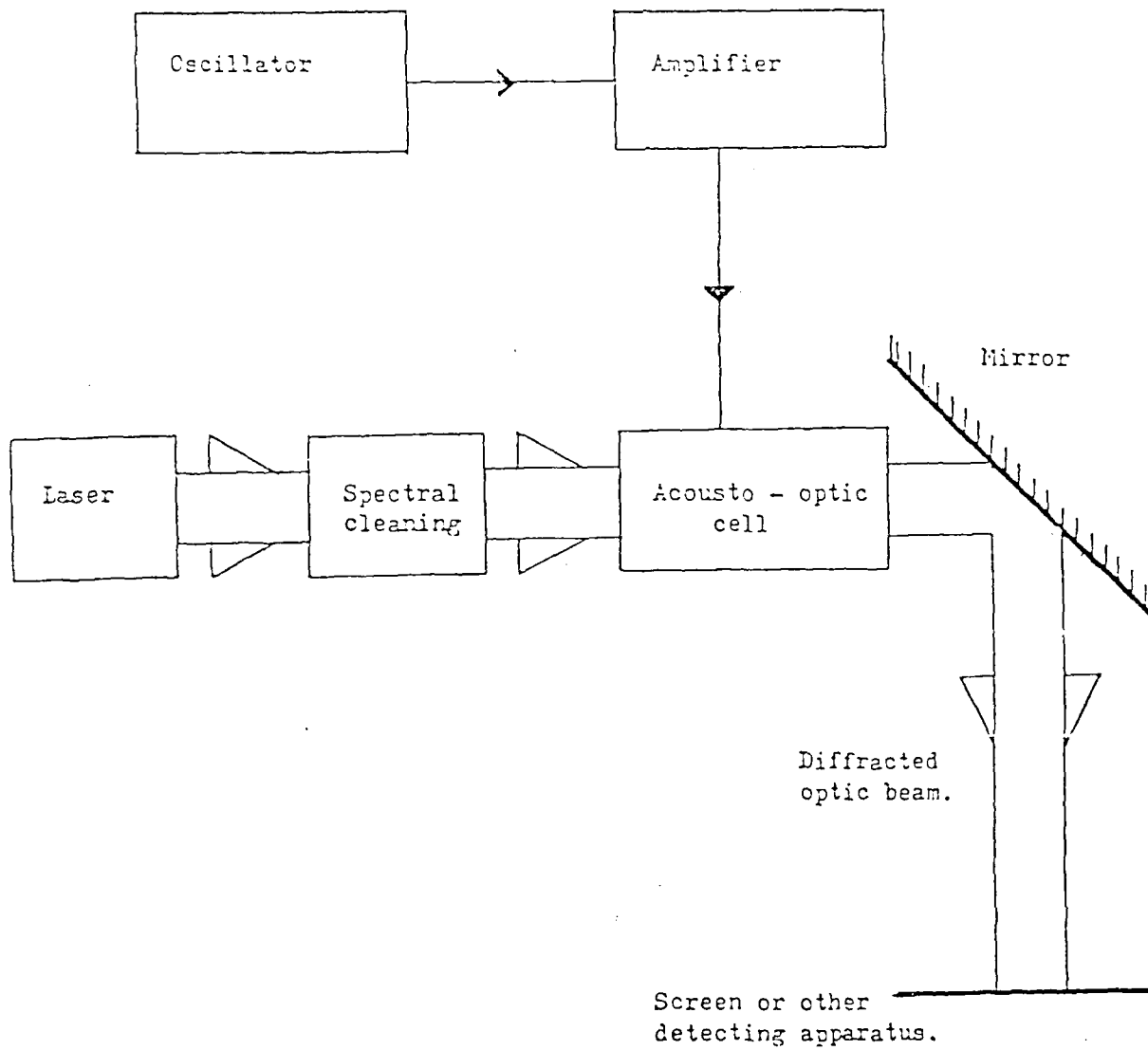


Figure 19. Deflection angle as a function of frequency. Laser at normal incidence.

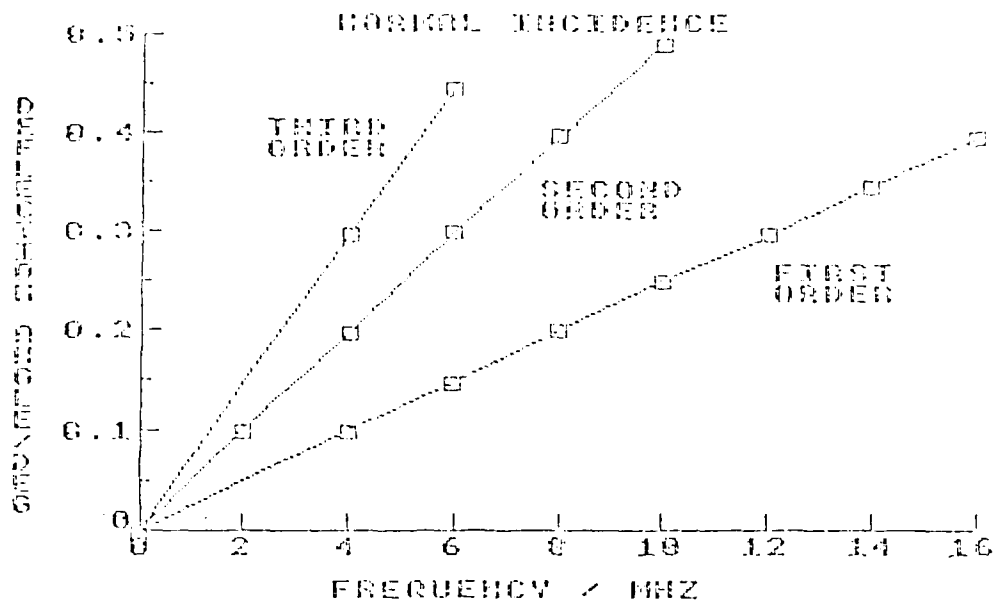


Figure 20. Deflection angle as a function of frequency. Laser incident at the Bragg angle.

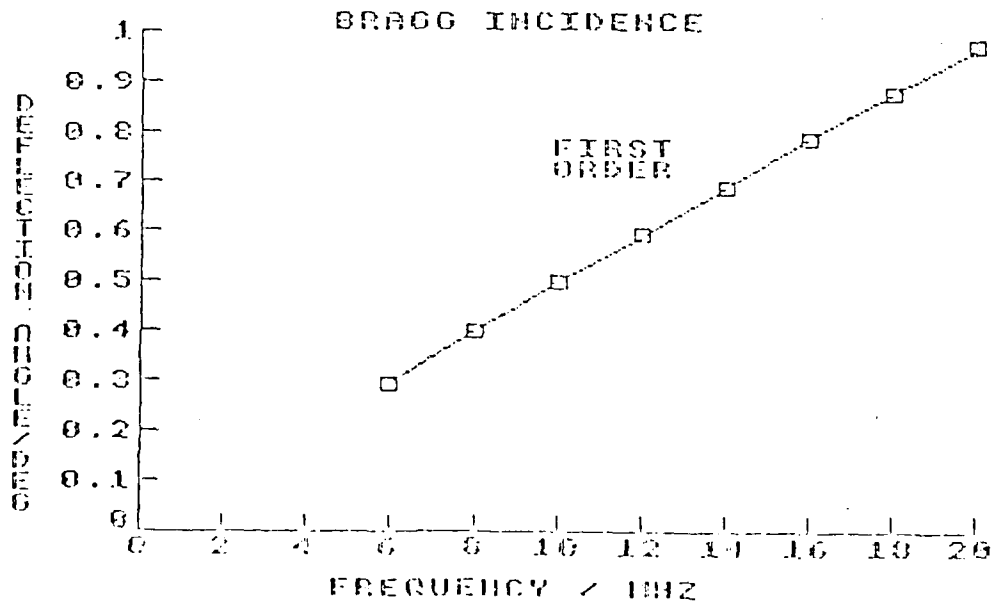


Figure 21. Deflected power as a function of sound frequency for light incident at normal and Bragg incidence.

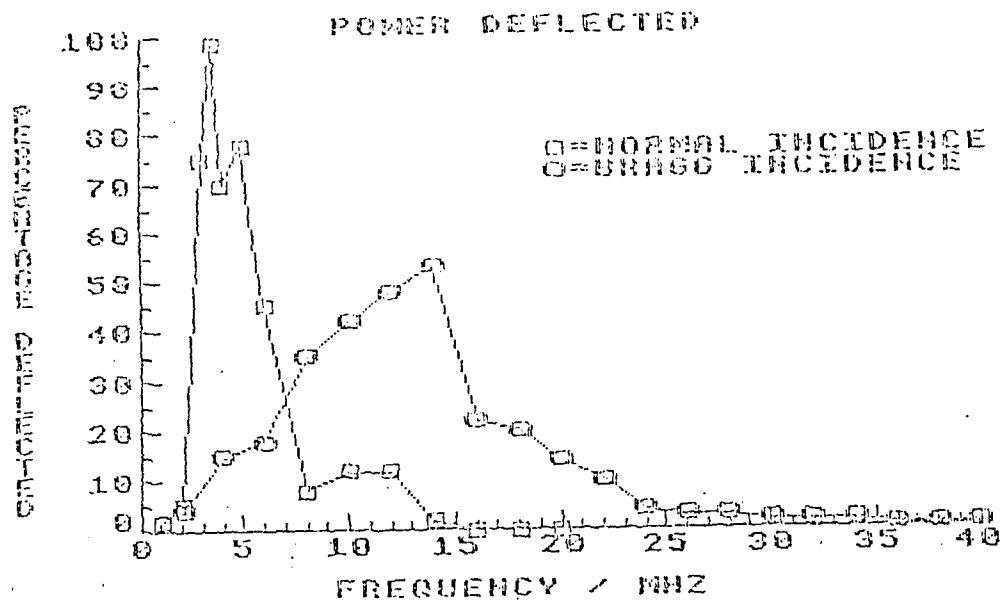


Figure 22. Series of photographs of diffraction pattern for various sound frequencies. Light at normal incidence.

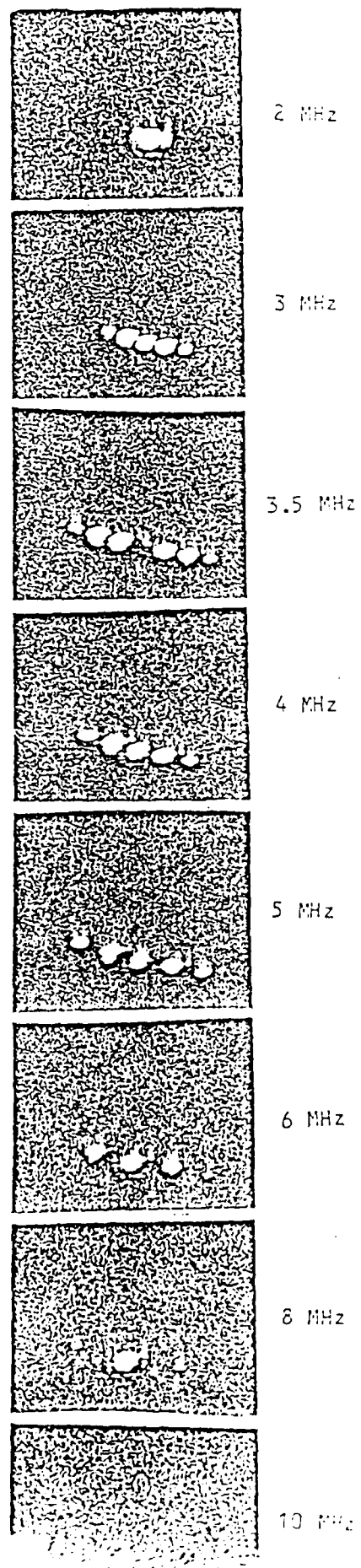
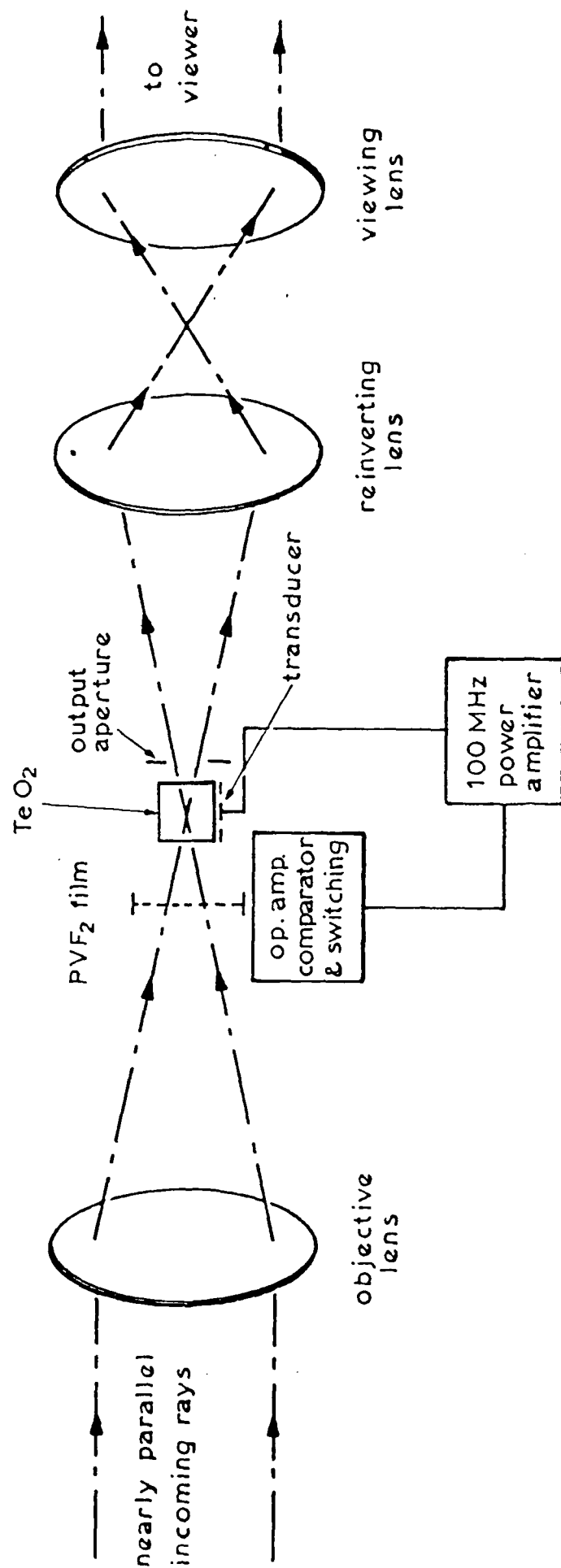


Figure 23. Integrated detector / deflector system.



FILMED
58